JOURNAL OF PETROLOGY

Journal of Petrology, 2018, Vol. 59, No. 11, 2093–2122
doi: 10.1093/petrology/egy092
Advance Access Publication Date: 11 October 2018
Original Article

OXFORD

Shrinkage Bubbles: The C–O–H–S Magmatic Fluid System at San Cristóbal Volcano

P. Robidoux[1]*, M. L. Frezzotti[2], E. H. Hauri[3†] and A. Aiuppa[4,5]

[1]Universidad Mayor, Escuela de Geología, Manuel Montt 367, Santiago, Chile; [2]Department of Earth and Environmental Sciences, University of Milano Bicocca, Piazza della Scienza 4, 20126 Milano, Italy; [3]Department of Terrestrial Magnetism, Carnegie Institution of Washington, 5241 Broad Branch Rd. NW, Washington, DC 20015, USA; [4]DiSTeM, University of Palermo, Via Archirafi 36, 90123 Palermo, Italy; [5]Istituto Nazionale di Geofisica e Vulcanologia (INGV), Sezione di Palermo, Via Ugo La Malfa 153, Palermo 90146, Italy

*Corresponding author. Telephone: +56951232150. E-mail: robidouxphilippe@gmail.com
[†]Deceased.

Received May 10, 2017; Accepted September 24, 2018

ABSTRACT

New analytical results for the composition of shrinkage bubbles (0·9–7·0 vol. %) in olivine-hosted (Fo <80%) primary melt inclusions (MIs) have been incorporated into a novel geochemical model for San Cristóbal volcano, Nicaragua. The vapour, liquid, and mineral components found inside shrinkage bubbles may represent relics of early C–O–H–S fluids exsolved from a magmatic-hydrothermal system. This conclusion is supported by high-resolution Raman microspectroscopy revealing: (1) gaseous CO_2 (d = 0·17–0·31 g/cm^3 in 31 samples) coexisting with liquid H_2O (in seven samples) at ambient temperature (<22°C) inside the shrinkage bubbles of naturally quenched inclusions; (2) several mineral phases (i.e. Fe, Cu-sulfides, Ca-sulfates and Mg-carbonates) formed along the bubble–glass interface, as confirmed by electron backscattered/energy-dispersive spectroscopy. The presence of liquid water was revealed by applying a novel subtraction method to fitted Raman spectra that isolated an isosbestic liquid-water band at 3460 ± 60/cm^{-1} (mean ± SD). In MIs, the major oxide composition of glasses containing shrinkage bubbles were analysed by electron microprobe, whereas glass volatile contents were measured with nanoscale secondary-ion mass spectroscopy. According to the water content of the glass inclusions (≤ 3·3 wt %) and the presence of liquid water at the bubble–glass interface, only small amounts of water (0·3 wt %) appear to have migrated inside the bubbles. From pre-eruptive (up to 1200°C) to post-eruptive temperatures, aqueous fluids represent the principal agents for chemical reactions inside MI bubbles involving dissolved ionic species (e.g. SO_4^{2-}, CO_3^{2-}, and Cl^-) and major and/or trace elements from the inclusion glass (e.g. Mg, Fe, Cu, Si, Al, Na, and K). After the initiation of nucleation (1009–1141°C), the volume of shrinkage bubbles expands and the surrounding glass contracts (at <530°C). The Fe–Mg–Cu-rich (vapour) shrinkage-bubble paragenetic mineral sequence formed during different cooling stages: (A) high-temperature sulfide precipitation at 500–700°C; (B) low-temperature magnesite precipitation at hydrothermal conditions <350°C; and finally (C) low-to-ambient temperature precipitation of carbonates and sulfates in liquid water at <150°C. Our findings indicate that the C–O–H–S fluids in shrinkage bubbles can represent an ideal preserved/closed magmatic-hydrothermal system evolving after the exsolution of magmatic fluids during cooling.

Key words: shrinkage bubble; melt inclusions; Raman spectroscopy; San Cristóbal; copper

INTRODUCTION

Recent studies have shown that up to 90% of the CO_2 budget in melt inclusions (MIs) can diffuse into the shrinkage bubbles because of the low solubility of CO_2 in silicate melts (e.g. Hartley *et al.*, 2014; Moore *et al.*, 2015 and references therein; Wallace *et al.*, 2015). As a consequence, those geobarometers that are widely employed when developing solubility models are not precise for bubble-bearing MIs, if the amount of CO_2 in the shrinkage bubbles is ignored (Lowenstern, 1995; Esposito *et al.*, 2011, 2014; Esposito, 2012; Lowenstern, 2015; Moore *et al.*, 2015). The original CO_2 budget in MIs at trapping conditions is generally re-estimated by adding the CO_2 content of the shrinkage bubbles to that contained in the glass. Riker (2005) showed that the relationship between the volume of a vapour bubble (10^1–10^4 cm^3) and the fraction of initially dissolved CO_2 lost to the bubble represents an excellent tool for estimating the pre-eruptive bubble size for Hawaiian tholeiitic MIs at Mauna Loa. More recently, novel techniques have been used to calculate the original CO_2 budget of MIs by using heating experiments (Mironov *et al.*, 2015) and measurements of CO_2 densities in the bubbles using Raman microspectroscopy (Esposito *et al.*, 2011). The loss of CO_2 to shrinkage bubbles was corrected for using a similar technique by Hartley *et al.* (2014), also using CO_2/Nb proxies for undegassed melts to correct for bubble-free inclusions in the AD 1783–1784 Laki eruption in Iceland. A combination of spectroscopy and experimental heating techniques has also been applied at Fuego (Guatemala), Seguam (Alaska, USA), and Kilauea Iki, and Kapoho (Hawaii) (Moore *et al.*, 2015; Wallace *et al.*, 2015; Tuohy *et al.*, 2016). These approaches, tested in different tectonic settings, have recently been applied by Aster *et al.* (2016) to cinder cones in the Cascades (Basalt of Round Valley Butte and Basalt of Old Railroad Grade) and the Trans-Mexican Volcanic Belt (Jorullo, Parícutin). Mironov *et al.* (2015) proposed a new method for analyzing the original CO_2 content of bubble-bearing MIs that involved applying heating and hydration experiments with a piston cylinder to olivines from the Bulochka vent at Klyuchevskoy volcano (Kamchatka, Russia).

At San Cristóbal volcano, in the Central American Volcanic Arc (CAVA; Nicaragua), combined Raman microspectroscopy and ideal-gas law (IGL) calculations have yielded corrected CO_2 concentrations of 718–1889 μg/g in MIs containing a shrinkage bubble (Robidoux *et al.*, 2017). In a different group of bubble-free MIs from the same olivine-host, the measured CO_2 concentrations were lower (71–527 μg/g) when directly measured with nanoscale secondary-ion mass spectroscopy (nano-SIMS). This indicated that the loss of CO_2 was controlled by deep degassing. Instead, a maximum concentration of ~5000 μg/g CO_2 for the undegassed melt was estimated by using the CO_2/S_{tot} value (with total sulfur determined as $SO_2 + H_2S$) from the Multi-GAS central plume survey (= 3·8) multiplied by the parental melt S content of ~1300 μg/g (e.g. Aiuppa *et al.*, 2014; Robidoux *et al.*, 2017). Those authors also estimated the minimum depth intervals of the magma plumbing system at San Cristóbal (3·4–7·4 km) using solubility models that integrated the first direct measurements of the contents of major volatiles, including H_2O, S, and Cl, determined in the silicate glass inclusions by nano-SIMS ion probe analysis. The results of major element analyses by electron microprobe (EMPA) on MIs and their olivine-host crystals were initially reported in Robidoux *et al.* (2017). This data set incorporated a corrected percentage of MgO from olivine added to each MI by taking into account the effects of post-entrapment crystallization (PEC) (Danyushevsky and Plechov, 2011). The compositions of volatiles in MIs included their CO_2 content, corrected by considering different fluid-density models.

Although most studies concentrate on the determination of the original CO_2 budget of MIs, recent investigations have revealed that additional magmatic volatiles, including multiple vapour/fluid phases in the C–O–H–S system (Kamenetsky *et al.*, 2007; Esposito *et al.*, 2016 and references therein) and halogens (e.g. Webster, 1992), can be present in MI shrinkage bubbles. Thus, water and sulfur, chlorine, and fluorine species should also be expected in shrinkage bubbles, along with variable associations of dissolved ions such as Si, Al, Ca, Mg, and Fe (Kamenetsky *et al.*, 2007). Carbonates are frequently observed in shrinkage bubbles. Thus, reliable estimates of the total CO_2 budget in MI bubbles also depends on how much CO_2 is sequestered in the carbonates precipitated at the bubble–glass interface by exsolved fluids at high magmatic temperatures, or during successive cooling by the diffusion of CO_2 in MI (Kamenetsky *et al.*, 2002; Kamenetsky & Kamenetsky, 2010 and references therein; Moore *et al.*, 2015).

Water in shrinkage bubbles has been considered by Lowenstern (1995), Kamenetsky *et al.* (2002), Esposito *et al.* (2011, 2016), Moore *et al.* (2015), and Wallace *et al.* (2015). Liquid water was detected by Esposito *et al.* (2016) at the bubble–glass interface in re-heated MIs. The contrasting diffusion rates of CO_2 and H_2O (Sobolev & Danyushevsky, 1994; Hauri *et al.*, 2002; Gaetani *et al.*, 2012) could make the presence of water in bubbles important for understanding the real concentration or mass of volatiles originally trapped in the MIs (Esposito *et al.*, 2016). Additionally, the mineral phases (e.g. hydrous and anhydrous carbonates and sulfur species) detected on the bubble walls (Kamenetsky *et al.*, 2001, 2002, 2007; Moore *et al.*, 2015; Esposito *et al.*, 2016) are probably precipitated from C–O–H–S fluids in the vapour bubble.

The objective of the present study is to characterize the evolution of major C–O–H–S volatiles during and after the formation of shrinkage bubbles in naturally quenched MIs from olivines in tephra from San Cristóbal volcano. A detailed description of inclusion textures and petrographic observations based on the distribution of primary MIs (Roedder, 1979, 1984;

Frezzotti, 2001) in the olivine phenocrysts is presented. Combining scanning electron microscopy (SEM) and Raman microspectroscopy makes it possible to define the volatile chemical systems, and particularly the role of CO_2, by proposing new methodological considerations for estimating the budget of volatiles. Particular attention is paid to identifying the water and mineral precipitates inside the bubbles. There have been many studies of the variations in the water content in melt inclusions from volcanic arcs (see Plank *et al.*, 2013), and these need to be evaluated further via an extensive revision of the MI chemistry by EMPA and nano-SIMS (e.g. Danyushevsky *et al.*, 1993; Sisson & Layne, 1993; Sobolev & Chaussidon, 1996; Hauri *et al.*, 2002; Sadofsky *et al.*, 2008). Evidence from San Cristóbal samples and the literature (e.g. Robidoux *et al.*, 2017) supports the need to reassess the H_2O, S, and Cl contents in degassing models when the Raman-corrected content of CO_2 is involved. Further, water represents a principal agent for chemical reactions (alteration) between dissolved ionic species (e.g. SO_4^{2-}, CO_3^{2-}, and Cl^-) and major elements (e.g. Mg, Fe, Cu, Si, Al, Na, and K). A new set of mineral identification data in the present study leads to two new models of vapour-bubble C–O–H–S-Cl fluid formation related to mineral paragenesis and physical mechanisms of bubble formation in MIs for void shrinkage bubbles and shrinkage bubbles containing fluids. These models can improve our understanding of the origin of sulfide mineralization in volatile-saturated magmas during and following eruptions. Processes occurring in shrinkage bubbles are explored here, mainly by discussing vapour–brine mineral phase analogues in porphyry–copper epithermal systems.

San Cristóbal volcano

San Cristóbal is a large ($\sim$107 km^3) and relatively young ($\sim$160 $\pm$ 60 ka) stratovolcano, located at 12°70′ lat. N. and 87°00′ long. W., northwest of the Cordillera de los Maribios, on the northwestern margin of the Nicaragua volcanic arc segment (Fig. 1) (Carr *et al.* 2007). The volcanic arc segment of Nicaragua includes a 25–34 km thin continental crust and limits the boundary where the oceanic Cocos Plate subducts under the Caribbean Plate with the highest angle of slab dip (65–75°) among the whole Central American Volcanic Arc (CAVA). CAVA represents the continuity of the subduction zone and the chain of volcanoes extending along the Pacific coastline between Guatemala and Costa Rica (Demets, 2001). The active CAVA volcanoes are geographically distributed along a northwest-oriented, 1100 km long corridor between latitudes 10 and 15°N, and are composed of Quaternary edifices of diverse morphology, including composite volcanoes, calderas and monogenetic cinder cones (McBirney & Williams, 1965; Walker *et al.*, 2001) (Fig. 1).

San Cristóbal is currently a continuously (passively) degassing open-vent volcano (e.g. Aiuppa *et al.*, 2014), but its common activity is dominated by cycles of lava emissions, intermittent strombolian to moderate vulcanian explosions generating significant fallout and pyroclastic deposits, and occasionally some rare pumice-bearing sub-plinian eruptions (Hazlett, 1977, 1987; Havlicek *et al.*, 1999, 2000). Erupted volcanic rocks include basalts, basaltic andesites and dacites (Martinez & Viramonte, 1971; Hazlett, 1977, 1987; Carr, 1984; Carr *et al.*,1990; Patino *et al.*, 2000; Bolge *et al.*, 2009; Heydolph *et al.*, 2012). San Cristóbal volcano has been in a period of reactivation since 1971, with dominant basaltic andesite eruptive products, which also characterized the eruptive cycle of the 16–17th centuries (Hazlett, 1987).

MATERIAL AND METHODS

Collected field samples

On May 3, 1971, after three centuries of dormancy, San Cristóbal reactivated with intense summit crater degassing and finally exploded in March 1976 with a moderate vulcanian eruption and several phreatic eruptions (Hazlett, 1977). The products of these eruptions (Fig. 2a), were mainly scoria of medium to coarse lapilli, of a dark grey to black colour (SC02B). Coarse ashes of dark to grey tones contain most of the loose olivine phenocrysts (0·5–2·0 mm) selected for this study; subordinate clinopyroxene phenocrysts were also observed in the tephra. Subordinate lithic fragments (<5%), mostly beige-golden pumice fragments, were mixed with the juvenile material.

During 1680 and 1684–1685, a complex eruptive cycle involved emission of spatter agglutinated lava bombs, followed by smaller grain size scoria deposits (outcrop SC5; Fig. 2b and c). Among those reworked, mixed coarse ashes, a layer of coarse ashes and small lapilli-sized scoriae (sample SC5K) that contained several lithic fragments, including abundant pumices of different colours (<15%), was selected. SC5K, laid on top of the entire SC5 sequence, is composed of several volcanic and volcanoclastic layers deposited from the Holocene to the 16–17th century period (Fig. 2b and c).

Eruptions were characterized by short to long-term strombolian to vulcanian, and even plinian, activity, during the Holocene at San Cristóbal (Hazlett, 1987; Havlicek *et al.*, 2000). At the base of outcrop SC5, was found the layer SC5C made of coarse ashes and homogenous lapilli-sized scoria of dark tone. SC5D is a layer found on top of SC5C with continuous contact. It represents a part of the Escoria-Negra-Ashes-and-Block (ENAB) deposit (Havlicek *et al.*, 1999, 2000), which symbolizes a vulcanian explosion with primitive composition, characterized by volatile-rich MIs (Robidoux *et al.*, 2017). Another primitive composition layer was identified, previously sampled and studied for the volatile content in MIs (Robidoux *et al.* 2017), on the Block-and-Ashes (BA) deposit (Havlicek *et al.* 2000). The SC11 outcrop represents this layer and it is located 600 m south of the crater rim (Fig. 2d). The sequence initiated with a layer of coarse scoriae and bombs and a thick avalanche

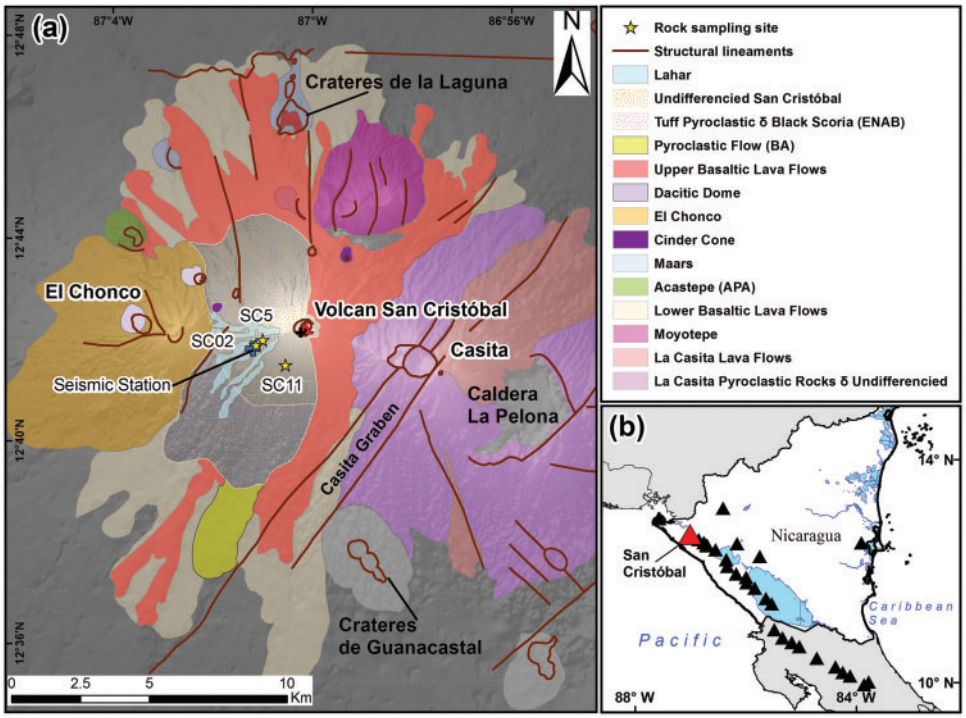

Fig. 1. Maps of rock sampling sites. (a) Map of the main lithostratigraphy in the San Cristóbal-El Chonco-Casita area based on the SRTM (resolution 10 metres) digital elevation model provided by INETER. Contours are based on Havlicek *et al.* (2000) and Hazlett (1977, 1987). Lahar contours, brown lineaments representing regional structures and the GPS coordinates of the seismic station are all from INETER. (b) Regional map of Nicaragua and the San Cristóbal location. Hydrographic layers of Nicaragua and continent contour shape files are from ESRI and mapped with ArcGIS (Arc Map 10·1, World Map).

block layer. Following and mixed with the avalanche deposit was found the juvenile material SC11D, which was made of glassy porous medium to large lapilli-sized scoriae and unconsolidated coarse ash.

Sample selection

Samples were studied in key scoria layers from historic-present eruptions (SC02B and SC5K) and also from ENAB (SC5C and SC5D) and BA (SC11D) Holocene deposits. The materials collected from each layer were dried in an oven at 60°C for 48 h to remove any moisture and then sieved into different grading sizes. Olivine crystals were handpicked from the 0·5 to 1 mm sieved fractions of sampled ash and scoria. Such small diameters were selected because, in larger fragments with olivines a significant fraction of the water from any MI could have been lost by diffusion through the host mineral (Lloyd *et al.*, 2013).

The present study focuses on primary MIs in olivine crystals that are representative of undegassed magmas. The MIs were grouped based on petrographic studies (Clocchiatti, 1975; Roedder, 1984; Goldstein, 1993; Goldstein and Reynolds, 1994; Frezzotti, 2001; Bodnar, 2003; Goldstein, 2003) and morphological studies (e.g. geometric shapes and sizes, and bubble dimensions; Clocchiatti, 1975; Frezzotti, 2001). This approach is based on a systematic analysis of textural features of MIs in 100 crystals of olivine within each layer to verify the homogeneity of petrographic features among the different volcanic deposits (Fig. 3; Supplementary Data Electronic Appendices 1 and 5; supplementary data are available for downloading at http://www.petrology.oxfordjournals.org). When textural and chemical characteristics observed for a group of MIs suggest near-contemporaneous trapping during the growth stages of olivine, the term 'population' is used (Roedder, 1979; Frezzotti, 2001). Whisker-and-box diagrams (Fig. 4) are presented to summarize the main characteristics of single MI populations, including the concentrations of volatiles in the glass and the bubble volume (see Esposito *et al.*, 2014). This approach integrates both qualitative and quantitative textural characteristics and facilitates the understanding of the number of events leading to MI trapping during olivine growth. The terminology referring to MI trapped during a single event as 'MI assemblages' (Roedder, 1979; Bodnar, 2003) was not applied in the present study, since classifying a MI assemblage requires also knowledge of the temperature and pressure conditions of trapping. Heating or pressure experiments were not performed in this study to preserve crystallization and chemical diffusion processes occurring inside the bubbles upon natural cooling.

The primary origin of MIs was assessed based on their distribution along crystal growth surfaces (Roedder, 1979). MIs showing zonal arrangements were targeted to provide reliable descriptions of sectioned shrinkage-bubble-holding inclusions (Anderson, 1974, 2000; Bodnar & Student, 2006).

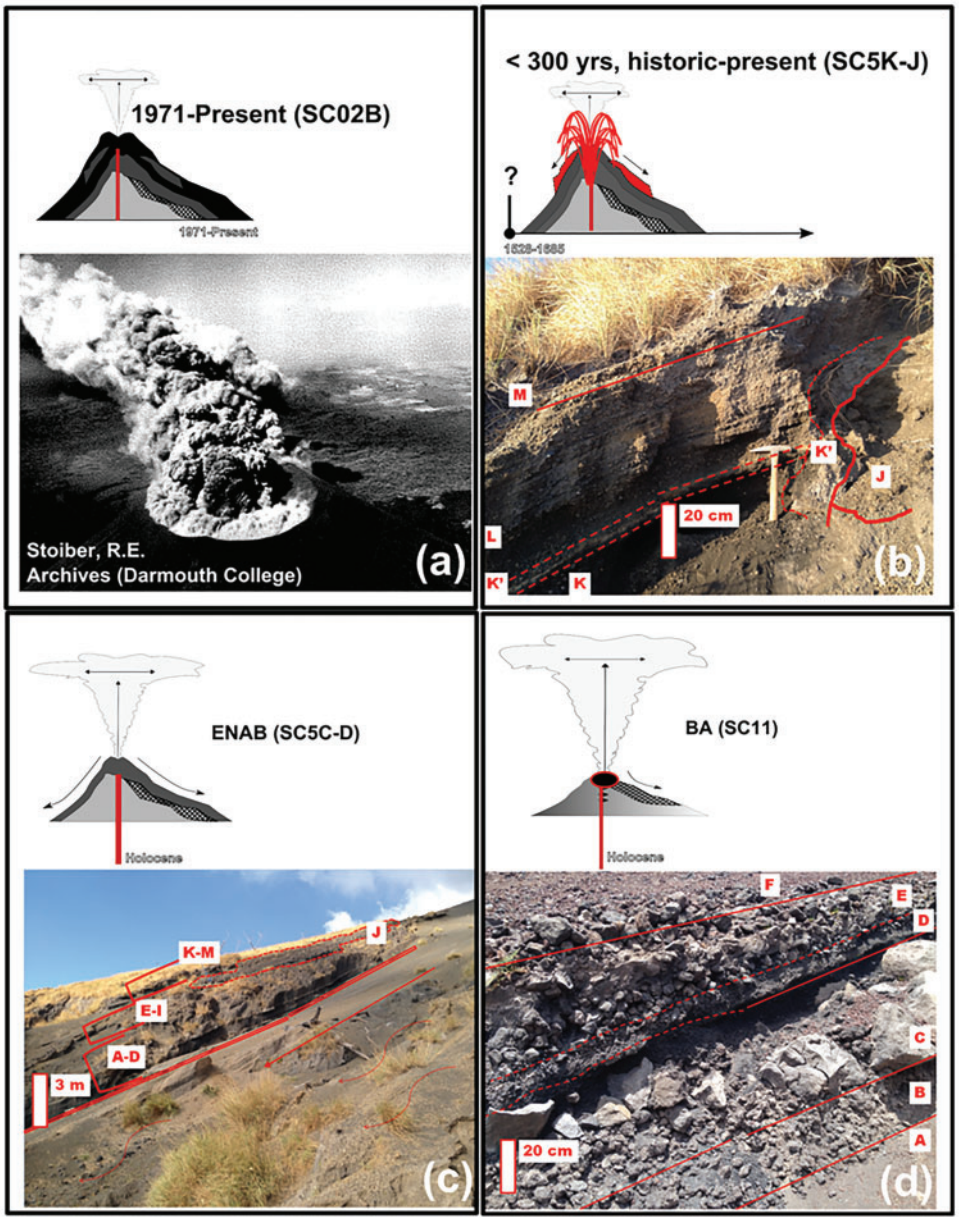

Fig. 2. Studied eruptions from San Cristóbal. (a) Photography of the March 1976 explosive eruption (VEI = 2), which resulted in the deposition of layer SC02B. Modified from Stoiber (2001). (b) SC5K layer caps the whole SC5 outcrop and is limited by a maximum age of ~300 years. (c) SC5 is a series of layers composed of several pyroclastic and volcanoclastic layers deposited during the Holocene up to the 16th and 17th centuries. The studied layers SC5C and SC5D are from Escoria Negra ashes and block (ENAB) (Havlicek *et al.*, 2000). (d) SC11 outcrop represents the block-and-ash (BA) deposit (Havlicek *et al.*, 2000). Stratigraphic layers are coded in alphabetical order as in Robidoux *et al.* (2017).

We applied Raman microspectroscopy to test for the migration of C–O–H–S volatiles from the melt to the shrinkage bubble that is expected to occur on the basis of magmatic pressure and temperature conditions (Moore *et al.*, 2015; Wallace *et al.*, 2015). Most bubbles inside MIs resulted from cooling that leads to thermal contraction of the melt (Roedder, 1979; Lowenstern, 1995), or by volatile exsolution from the melt (Roedder, 1979; Skirius *et al.*, 1990; Anderson & Brown, 1993; Cervantes *et al.*, 2002). A bubble which was formed strictly in response to equilibrium conditions in the trapped homogeneous melt and saturated in a low-density fluid phase after depressurization and cooling was considered a shrinkage bubble (Lowenstern, 1994). In that case only, the amount of CO_2 from the newly-formed bubble inside the natural MI could have been reintroduced into the total budget of the original MI by applying different approaches (Riker, 2005; Esposito *et al.*, 2011; Hartley *et al.*, 2014; Aster, 2015; Moore *et al.*, 2015; Wallace *et al.*, 2015; Aster *et al.*, 2016; Robidoux *et al.*, 2017).

The studied olivine phenocrysts frequently contain groups of primary MIs distributed along growth zones (Sobolev & Kostyuk, 1975; Roedder, 1979). These

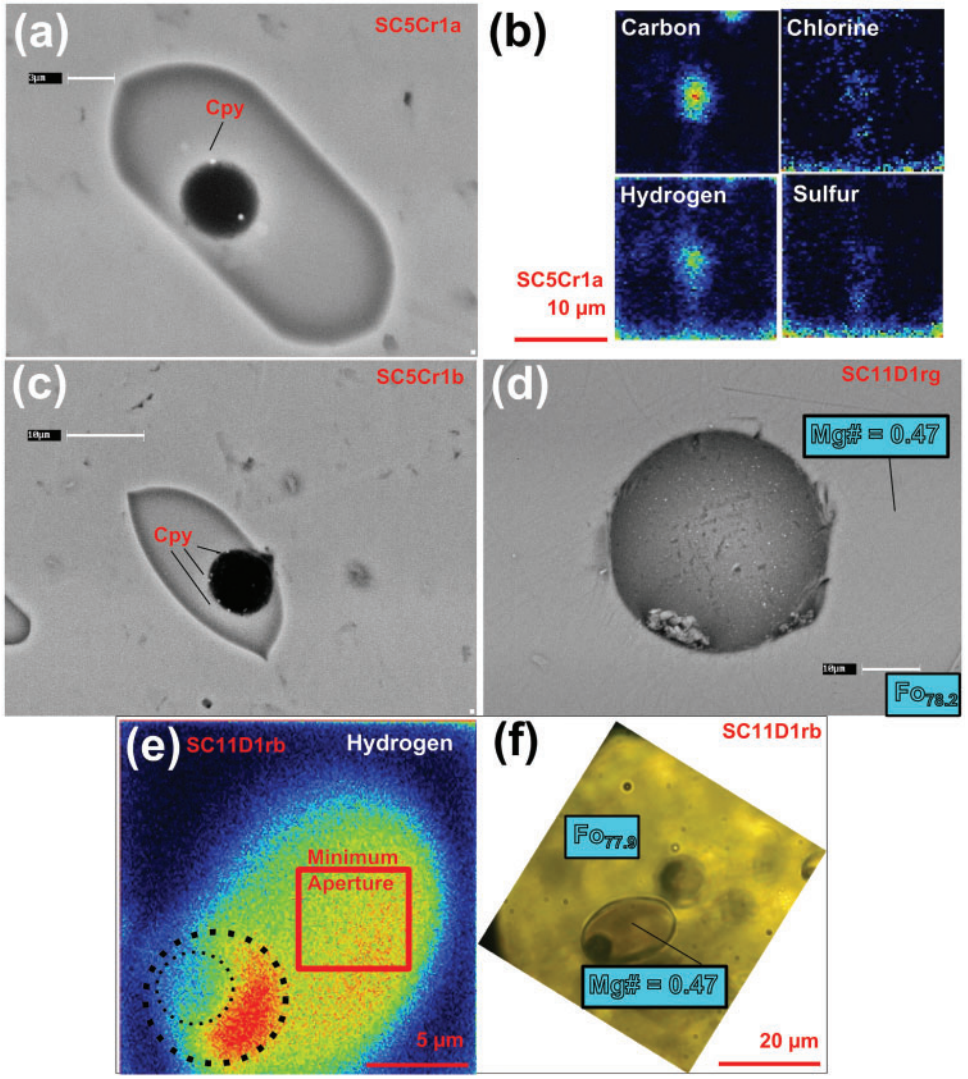

Fig. 3. Images of glass inclusions with their bubbles. (a) SEM image of chalcopyrite (Cpy) inside a shrinkage bubble made with X-ray scanning, energy dispersive spectroscopy EDS, sample SC5Cr1a. (b) Nano-SIMS map of volatile element intensity ratios (hydrogen, carbon, sulfur, chlorine) to silicon (^{30}Si), sample SC5Cr1a. The carbon signal at the center of the bubble may come from contamination by the diamond powder filling the open bubble space, or possible spatial variations caused by textural heterogeneities. (c) SC5Cr1b, ibid. to SC5Cr1a. (d) SEM image of MI in SC11Dr1g sample (without shrinkage bubble). (e) Nano-SIMS map of hydrogen intensity in SC11Dr1b, showing the absence of a carbon signal in the bubble. Minimum Nano-SIMS aperture is shown for this inclusion, but it can be 2·5 µm x 2·5 µm (f) High-magnification image of SC11Dr1b. Fo % contents are reported for each mineral.

inclusions were selected because they trap juvenile melts and, therefore, can hold an authentic shrinkage bubble. The ideal silicate inclusion that contains a shrinkage bubble is thus a closed chemical system and has a glassy texture; it is recognized by its spherical and rounded ellipsoidal shape (no angular borders). Post-entrapment daughter crystals and post-entrapment crystallization (PEC) on the MI walls should be avoided, since they can alter the silicate composition (Lowenstern, 1995 and references therein).

Selecting MIs with representative shrinkage bubbles was very important when performing the textural study (Table 1; Supplementary Data Electronic Appendix 3). The volume fraction of the bubble relative to the entire glass inclusion needs to be consistent between the analysed inclusions (Anderson & Brown, 1993), particularly for several inclusions that constitute the same population for multiple olivine hosts. A low volume percentage of the vapour bubble relative to the glass inclusion ($\ll$5%) is also an excellent index (Anderson & Brown, 1993; Lowenstern, 1994).

Sample preparation

The selected olivine crystals were prepared in CrystalBond^{TM} over thin sections. Glasses from MIs were exposed at the olivine surface on one side for analysis by Raman microspectroscopy. The crystal samples on the thin sections were sequentially polished with diamond powder of sizes 6, 3, and 1 µm

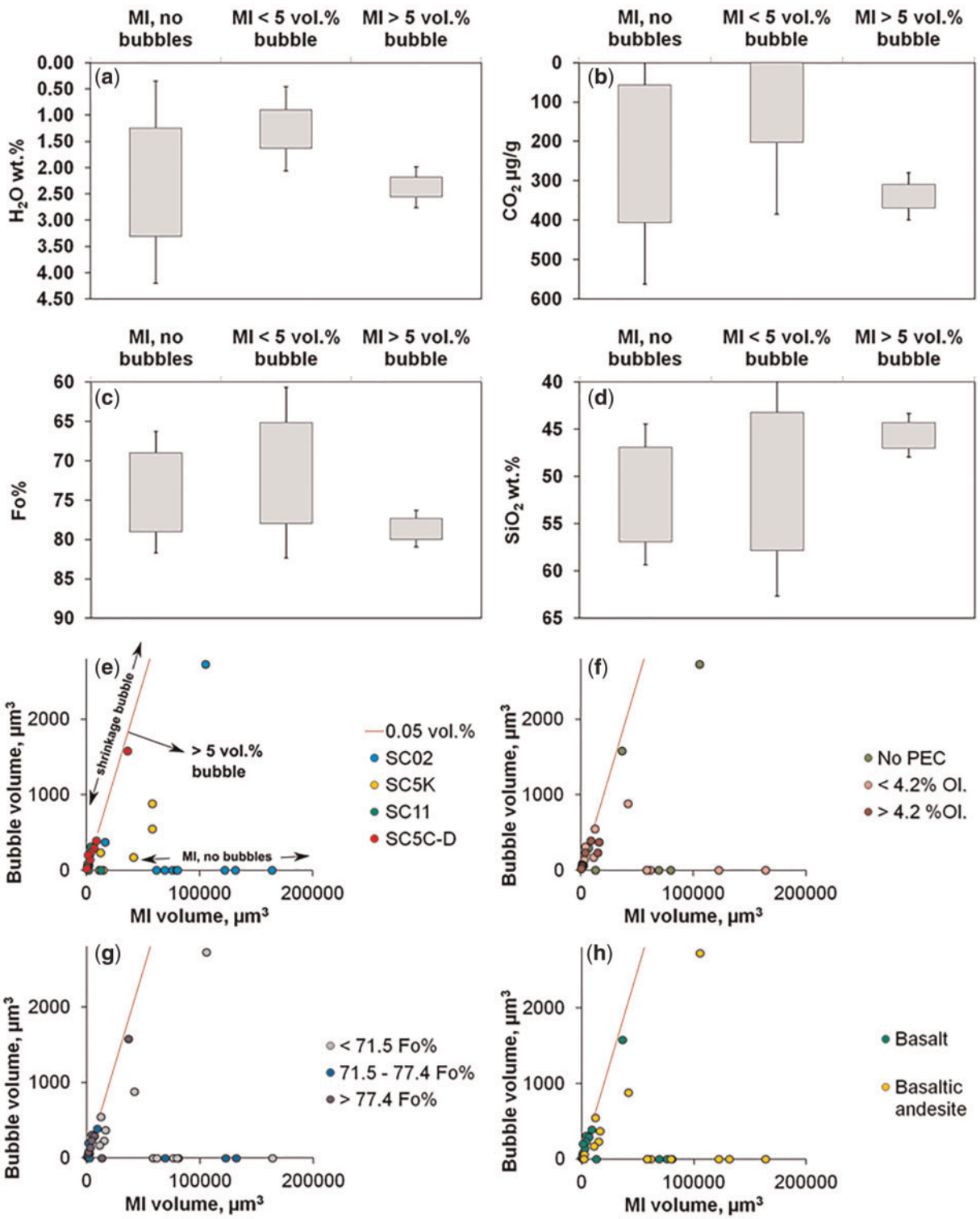

Fig. 4. Whisker-and-box diagrams of the geochemical parameters and measured bubble volume as functions of the MI volume (μm^3) from San Cristóbal inclusions. Data ranges are attributed for each MI population (MI, no bubbles; MI bubble <5 vol. %; MI, bubble >5 vol. %) including the standard deviation values (error bars along the vertical boxes). (a) H_2O wt % content in MIs; (b) CO_2 µg/g content in MIs; (c) forsterite content (Fo %) in olivine hosts; (d) SiO_2 wt % content in MIs. Measured bubble volumes as functions of the MI volumes (in μm^3) are reported in the subsequent figures where groups of geochemical parameters are classified (quartiles); (e) MI stratigraphic layer; (f) percentage of olivine added (% Ol) for post-entrapment correction (PEC); (g) forsterite content in olivine hosts to MIs (Fo %); (h) MI composition with classification as basalt or basaltic andesite.

Table 1: Inclusion and bubble dimensions

Samples no.	Bubble* width, depth μm	Bubble* length μm	Bubble* Vol. cm^3	Melt Inclusion* width, depth μm	Melt Inclusion* length μm	Melt Inclusion* Vol. cm^3	Bubble Vol. %	Other	MI order assemblage	MI Group MI Population	Fo %
SC02B											
SC02Br3a1	6·0	5·7	1·04E-10	23·8	19·1	4·55E-09	2·3		A1/A3	AB	71·5
SC02Br3b1	13·3	13·5	1·28E-09	62·8	54·4	9·75E-08	1·3		A1/A3	AB	
SC02Br3c1	23·9	19·9	4·94E-09	86·3	65·1	1·91E-07	2·6		A1/A3	AB	
SC02Br3d1	15·9	8·7	6·25E-10	60·2	47·8	7·19E-08	0·9	2	A1/A3	AB	
SC02Br3e1	10·6	11·1	6·77E-10	40·8	36·7	2·88E-08	2·3	2	A1/A3	AB	
SC02Br3f1	9·7	9·0	4·09E-10	33·1	27·6	1·32E-08	3·1		A1/A3	AB	
SC02Br3g1	4·4	3·9	3·53E-11	18·0	14·9	2·08E-09	1·7		A1/A3	AB	
SC02Br3h1	5·6	5·5	8·90E-11	21·8	17·9	3·67E-09	2·4		A1/A3	AB	
SC02Br5a1	13·1	14·8	1·49E-09	52·2	49·3	6·64E-08	2·2	2, 3	A1/A2	AB	65·1
SC5k											
SC5k3Gb	10·1	10·2	5·23599E-10	39	52	4·14125E-08	1·3		A1/A3	AB	
SC5Kr3GA1	4·83	4·9	6·07209E-11	12·7	18·5	2·27586E-09	2·7		A1/A3	AB	69·4
SC5Kr3GB1	2·14	2·3	5·92745E-12	4·72	7·14	1·2599E-10	4·7	Oxide	A2/A3	AB2	
SC5kr5a1	12·0	11·8	8·77E-10	41·4	37·9	3·12E-08	2·8		A1/A1	AB	
SC5D											
SC5Dr1a1	9·1	8·3	3·26E-10	25·7	24·0	7·74E-09	4·2		A1/A2	AB	77·6
SC5Dr1b1	8·2	7·4	2·35E-10	24·8	18·4	4·39E-09	5·4		A1/A2	AH	77·6
SC5Dr1c1	6·6	7·5	1·96E-10	17·0	13·0	1·50E-09	13·1		A1/A2	AB	77·3
SC5Dr3a1	15·5	13·9	1·58E-09	54·5	35·9	3·67E-08	4·3		A1/A2	AB	79·5
SC5Dr3b1	11·5	10·7	6·90E-10	31·3	23·8	9·25E-09	7·5		A1/A2	AB	
SC5C											
SC5Cr1a1	3·8	3·5	2·38E-11	15·1	9·2	6·71E-10	3·5		A1/A2	AB	
SC5Cr1b1	5·0	4·4	5·00E-11	13·7	9·7	6·82E-10	7·3		A1/A2	AB	
SC5Cr1c1	2·8	3·4	1·71E-11	10·6	6·4	2·24E-10	7·6		A1/A2	AB	
SC5Cr1d1	2·9	2·8	1·18E-11	11·0	6·7	2·61E-10	4·5		A1/A2	AB	
SC5Cr1e1	5·9	6·8	1·44E-10	49·0	13·2	4·50E-09	3·2		A1/A2	AB	
SC5Cr1f1	7·4	6·7	1·73E-10	28·6	14·9	3·34E-09	5·2		A1/A2	AB	
SC5Cr4a1	7·0	6·7	1·64E-10	18·3	19·1	3·50E-09	4·7		A1/A2	AB	
SC5Cr4b1	5·8	6·1	1·11E-10	21·8	16·7	3·19E-09	3·5		A1/A2	AB	
SC5Cr4c1	5·4	5·0	6·96E-11	16·0	14·5	1·76E-09	4·0		A1/A2	AB	
SC11D											
SC11Dr1a1	10·5	9·5	4·95E-10	31·1	23·3	8·83E-09	5·6	2, 3	A1/A1	AB	77·4
SC11Dr1b1	8·6	8·3	3·09E-10	24·7	18·1	4·24E-09	7·3	2, 3	A1/A1	AB	77·9
SC11Dr1c1	7·2	6·5	1·61E-10	26·6	17·0	4·01E-09	4·0		A1/A1	AB	
SC11Dr1d1	8·6	7·9	2·83E-10	25·0	19·2	4·86E-09	5·8		A1/A1	AB	
SC11Dr4a1	8·5	7·6	2·60E-10	28·3	17·1	4·35E-09	6·0		A1/A1	AB	

[1]Ellipsoid, where depth equals shorter axis
[2]Deformed bubble
[3]Bubble squeezed on melt inclusion border

*All selected M.I. for Raman spectroscopy analyses are fully enclosed and only contain a bubble.
AB, same textural assemblage and stands for inclusion with bubble.
AH, same textural assemblage and stands for inclusion with bubble and oxide.

The same section mounts were carbon coated for SEM analyses. The SEM also allowed photographs of the bubbles to be taken using backscattered-electron imaging (Fig. 3a, c, and d). Different analyses by electron backscattering (using backscattered secondary-electron [BSE] imaging) and EDS X-ray scanning were also performed within intersecting bubbles in order to observe and identify the major elements that constitute the minerals formed at the bubble–glass interface.

The sample mounts were put in an ionized-water bath for washing and the crystals were repolished before being prepared for analysis using the 50/50 L nano-SIMS. During this step, the crystals were separated and pressed into indium inside a 25-mm-diameter disk before being washed and repolished by sequentially using diamond powder of sizes 3, 1, and finally 0·25 μm This cleaning process was essential because carbon contamination from the diamond powder used in nano-SIMS and in the coating used for polishing can interfere with the measurements. Once the surfaces were clean, the nano-SIMS analyses required the crystal surfaces to be coated with gold. After the measurements, the same indium mount containing the samples was transferred from the nano-SIMS device to the EMP device. The olivine crystals were kept on the same indium mounts, the gold coating was washed off and they were repolished by sequentially using diamond powder of sizes 3, 1, and 0·25 μm before being coated with carbon for the EMPA. In the EMP, EDS images were used to carefully check all areas that might have been affected by ions during the ion-beam bombardments during nano-SIMS measurements (Fig. 3a–c).

Raman spectroscopy

The Raman microspectrometer used is a Horiba Jobin Yvon high-resolution HR800 LABRAM at the Laboratorio di spettroscopia MicroRaman in the Dipartimento di Scienze della Terra (DST), University of Torino. The excitation source was a 532 nm green laser, with power at the emission source of 100 mW. Analyses were performed inside shrinkage bubbles (diameter 2 to 20 μm) of unexposed MIs with a confocal setup, with a resulting spot size of 1x1x3 μm (Supplementary Data Electronic Appendix 1). Instrumental calibration was performed daily based on the position of the silicon main vibration at 521 cm^{-1}. Spectral accumulations varied from 30 to 180 seconds and a minimum of 2 accumulations per spectrum were recorded (Table 2). Peak attribution has been made based on our database of reference spectra (e.g. Frezzotti *et al.*, 2012).

CO_2 density in the bubble

In shrinkage bubbles, CO_2 was revealed by the two characteristic bands of the Fermi doublet at 1285–1290 and 1388–1393 cm^{-1}, bounded by the hot bands (Fermi, 1931; Wright & Wang, 1973, 1975). The position of the two CO_2 Fermi bands was determined by fitting Gaussian/Lorentzian curves to the Raman spectra with Fityk 0.9.8 free software (Table 2). The distance between the Fermi doublet (Δ) bands shows a positive correlation with the CO_2 fluid density, which can be quantified (Fig. 5) (Wright & Wang, 1973, 1975). The error in the peak-fitting procedure was used to estimate the precision of Δ (cm^{-1}) using the wavelength of Fermi doublet splitting measured to two decimals (0.01 cm^{-1}), which covers the CO_2 precision of the Raman densimeter equation. A number of distinct experimental equations have been proposed to calculate CO_2 fluid density based on Δ spectral distances (in cm^{-1}; e.g. Rosso & Bodnar, 1995; Kawakami *et al.*, 2003; Yamamoto & Kagi, 2006; Song *et al.*, 2009; Fall *et al.*, 2011; Wang *et al.*, 2011). For San Cristóbal samples, the relation was best suited for application of the Fall *et al.* (2011) method for which the authors use a similar Raman spectral resolution (600 grating) at controlled temperatures (18–21°C) and peak-fitting functions (Gaussian/Lorentz).

H_2O presence in the bubble

Liquid water was detected in analyses collected at the bubble–glass border in the 2750–3900 cm^{-1} spectral region (Table 3; Fig. 6). The water Raman band observed in several spectra represents the O–H stretching mode of liquid water (Walrafen, 1964, 1967), The Raman spectrum of liquid water was revealed by the isosbestic point at 3460 ± 60 cm^{-1} (Walrafen, 1967), but in most shrinkage bubbles, overlapping bands were observed, resulting from vibrations of OH groups and H_2O molecules in glass (~3100–3750 cm^{-1}) and in liquid water (cf., Thomas *et al.*, 2006 and references therein). In order to spectrally resolve the contribution of the liquid water in mixed spectra and reveal its presence along the bubble–glass interface, we applied a multi-peak Gaussian fitting function using OriginPro8 software. After background subtraction, the bands of liquid water and glass water were thus revealed with a double Gaussian fitting function for each spectrum. The multiple Gaussian fitting curve at a maximum of 1825 a.u. of intensity (3460 ± 60 cm^{-1}) was chosen as the standard for liquid water (cf., Frezzotti *et al.*, 2012) and all other samples were normalized to this value (Fig. 6a; Table 4) (sample SC5Cr1f2 to which we attributed a 100% contribution of liquid water).

Nano-SIMS

CO_2, H_2O, S and Cl concentrations in glass inclusions from olivine hosts were determined using a Cameca NanoSIMS 50/50 L ion probe at the Carnegie Institution of Science using instrument settings explained in Robidoux *et al.* (2017). Sample/mount preparation procedures was also summarised in Hauri *et al.* (2002). Results for glass inclusions in this study are listed in Supplementary Data Electronic Appendix 2. Intensity area mapping was completed for numerous samples to detect any fractures and contamination (i.e. carbon from remaining diamond powder) in order to improve the choice of nano-SIMS spots. Due to possible textural

Table 2: Micro-Raman fluid density results with calculation parameters

Samples	Micro-Raman			Fluid density (g/cm^3)				CO_2 mass[1] g	Time acquisition (s)
	Fermi diad ν+ (cm^{-1})	Fermi diad ν+ (cm^{-1})	Δ (cm^{-1})	Wang *et al.* (2011)	Lamadrid *et al.* (2017)	Yamamoto & Kagi (2006)	Fall *et al.* (2011)		
SC02B									
SC02Br3a1	bdl	bdl	–	–	–	–	–	–	180
SC02Br3b1	bdl	bdl	–	–	–	–	–	–	180
SC02Br3c1	bdl	bdl	–	–	–	–	–	–	30
SC02Br3d1	bdl	bdl	–	–	–	–	–	–	30
SC02Br3e1	1288.016	1391.408	103.392	0.276	0.264	0.351	0.300	2.03194E-10	180
SC02Br3f1	bdl	bdl	–	–	–	–	–	–	180
SC02Br3g1	bdl	bdl	–	–	–	–	–	–	180
SC02Br3h1	bdl	bdl	–	–	–	–	–	–	180
SC02Br5a1	1289.617	1392.99	103.373	0.267	0.257	0.342	0.292	4.36417E-10	180
SC5k[2]									
SC5kr5a1	1288.02	1391.41	103.39	0.275	0.263	0.350	0.299	2.63E-10	360
SC5C									
SC5Cr1a1	1289.617	1392.99	103.373	0.267	0.257	0.342	0.292	6.94E-12	60
SC5Cr1b1	1289.617	1392.99	103.373	0.267	0.257	0.342	0.292	1.46E-11	180
SC5Cr1c1	1288.317	1391.408	103.091	0.142	0.157	0.222	0.171	2.91E-12	180
SC5Cr1d1	bdl	bdl	–	–	–	–	–	–	180
SC5Cr1e1	1288.317	1391.408	103.091	0.142	0.157	0.222	0.171	2.46E-11	180
SC5Cr1f1	1288.917	1391.408	102.491	0	0	0	0	–	180
SC5D									
SC5Dr1a1	1286·415	1389·828	103·413	0·286	0·272	0·361	0·310	1·01E-10	180
SC5Dr1b1	1286·415	1389·828	103·413	0·286	0·272	0·361	0·310	7·29E-11	180
SC5Dr1c1	1286·916	1389·828	102·912	0	0	0·161	0	1·93E-11	180
SC5Dr3a1	1286·415	1389·828	103·413	0·286	0·272	0·361	0·310	4·89E-10	180
SC5Dr3b1	1288·016	1389·828	101·812	0	0	0	0	–	180
SC11D									
SC11Dr1a1	bdl	bdl	–	–	–	–	–	–	180
SC11Dr1b1	bdl	bdl	–	–	–	–	–	–	180
SC11Dr1c1	bdl	bdl	–	–	–	–	–	–	30
SC11Dr1d1	bdl	bdl	–	–	–	–	–	–	180
SC11Dr4a1	bdl	bdl	–	–	–	–	–	–	180

[1]Fall *et al.*, 2011; [2]SC5Kr5a1 is used for CO_2 Raman corrections in the series SC5K (Robidoux, 2016).
bdl, below detection limit; -, empty results from calculation; 0, critical to limits from the densimeter range of value.
Decimal error from wavelength of Fermi Diad splitting is 0.001 cm^{-1}.

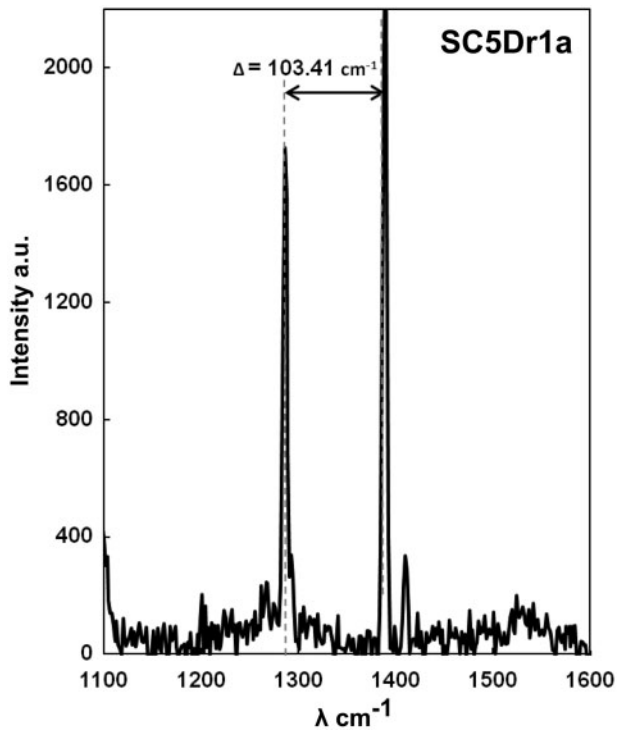

Fig. 5. Raman Fermi Diad peaks for CO_2. Example of CO_2 Fermi doublet distance interval (Δ; in cm^{-1}) measured in shrinkage bubble, sample SC5Dr1a.

effects in nano-SIMS imagery, the glass/border association of particular mineral phases and, or, the higher presence of volatiles, was only validated by SEM, EMP, and Raman spectroscopy (Fig. 3; Supplementary Data Electronic Appendix 1).

EMPA and LA ICP-MS

Major elements, Cl, and S contents in selected glass inclusions were determined using a JXA-8200 WD/ED combined electron microprobe (EMP; at INGV-Roma). The methodology, with the complete list of inclusions, groundmass glasses, crystals, results and analytical conditions, is summarized in Robidoux *et al.* (2017). In the present work, EDS mode was also used with EMPA to take images of the sample surface (Fig. 3) in order to select the glass area with the 'cleanest' surfaces. The concentrations of major oxides in selected MIs, corrected for PEC, from Robidoux *et al.* (2017) are given in Supplementary Data Electronic Appendix 3.

The concentrations of trace elements (Cu, Zn, Sc, and Pb) were added from larger MIs (>20 μm in diameter) after being analysed by laser ablation inductively coupled mass spectrometry (LA-ICP-MS) at the Istituto Nazionale di Geofisica e Vulcanologia (INGV), Sezione di Palermo (Supplementary Data Electronic Appendix 3). The analytical system consisted of an Agilent 7500 CX quadrupole mass spectrometer coupled with an ArF excimer laser ablation system (GeoLas Pro). After cleaning the surface of previous coating using ethanol, the same olivine indium mounts (Nano-SIMS, EMPA) were maintained in a He atmosphere during LA ICP-MS analysis, with a laser output energy of 10 J/cm^2, a repetition rate of 10 Hz, and a minimum 20 μm diameter circular spot. Errors for trace elements are <0·01 μg/g. Standards and procedures are explained in Correale *et al.* (2012).

RESULTS

Textural characteristics of melt inclusions

In olivine, primary melt inclusions (Roedder, 1984) were observed as zonal clusters, distributed following the growth zones in olivine phenocrysts (cf., Sobolev & Kostyuk, 1975; Roedder, 1979). They have ellipsoidal to rounded shapes; angular borders caused by olivine crystallization on the cavity walls were not observed. Inclusions have a variable length from 7 to >65 μm and contain bubbles with diameters between 3 and 20 μm

Six populations of olivine were identified, which were classified as groups 1 to 6 (G1–G6 in Supplementary Data Electronic Appendix 5, with G1 constituting olivines without observed inclusions). They showed distinctive textural characteristics and were defined as forming a specific MI population when textural and morphological parameters were repeatedly observed in a group of MIs (Supplementary Data Electronic Appendix 5).

About 100 olivine phenocrysts were studied in each of the sampled layers. The fractions of olivines with MIs containing a pure shrinkage bubble and glass (without oxides) in the SC11D, SC5C, SC5D, SC5K, and SC02B layers were 12%, 15%, 19%, 3%, and 4%, respectively; the corresponding fractions of olivines with MIs without a shrinkage bubble were 2%, 3%, <1%, 26%, and 5%, respectively. These findings reveal the eruptive sequence in which shrinkage bubbles most commonly nucleated. In addition, within single olivine crystals, MIs of a single population were of different size for most samples (Supplementary Data Electronic Appendices 1, 3 and 5). At the crystal core, glassy inclusions characterized most of the MI populations, whereas those at the rim were large honey-brown inclusions with dark bubbles. Bubble-bearing inclusions following clustered growth zones frequently appeared at either the rim or the core of phenocrysts within the same MI population.

For each studied layer, the relative proportions of MIs containing oxides were 38%, 36%, 53%, 71% and 86%, respectively. Larger glass inclusions (>30 μm) additionally contained variable amounts of microlites, some identified as clinopyroxene or plagioclase. Daughter olivine growing on the inclusion walls was detected in some inclusions with sizes <30 μm. In those cases, MIs were not selected for analyses. Overall, the vol. % size of trapped vapour bubbles (2–8%), of oxides (10–20%, mostly distributed along inclusion walls) and the distribution pattern of the sealed glass inclusions seems to be one of the most repetitive and distinctive features of MI populations G1 to G6 (Supplementary Data Electronic Appendix 5).

Table 3: Original and corrected H_2O-CO_2 contents of melt inclusions

	Original M.I.				Bubble		
Sample	H_2O wt %	CO_2 μg/g	°T_C °C, (CO_2)	°$T_{C\ (Avg.)}$ °C, (H_2O)	mass H_2O bubble (IGL) g	mass CO_2 bubble (IGL) g	mass CO_2 bubble (Raman) g
SC02Br3a	0·75	0·0	543	618	2·4E-12	0·0E + 00	3·1E-11
SC02Br3c	0·76	2	699	790	1·3E-10	2·3E-11	1·9E-09
SC02Br5a	1·36	89	597	707	2·5E-11	6·5E-11	1·6E-10
SC5Kr1a	1·63	71	530	643	1·5E-11	3·6E-11	6·9E-11
SC5Kr1b	1·51	202	489	591	3·5E-12	2·1E-11	1·5E-11
SC5k3Gb	2·16	191	536	676	5·7E-11	1·7E-10	1·6E-10
SC5Kr2a1	1·73	40	774	613	4·4E-12	5·0E-12	–
SC5Cr6	2·36	527	475	857	1·4E-11	3·0E-11	3·0E-11
SC11Dr1_2	2·91	386	651	656	4·2E-09	6·8E-09	–
SC11Dr1d	2·03	305	524	576	3·4E-11	8·7E-11	–
SC11Dr1g	2·25	310	448	576	6·4E-12	1·37E-11	–
SC11Dr1h	2·01	369	484	931	9·0E-12	1·45E-11	–
SC11Dr1i	2·05	350	455	607	5·6E-12	1·55E-11	–

	Corrected M.I.						
Sample	Glass Mass g	mass H_2O bubble g	Selected mass CO_2 Bubble[1] g	Corr. [H_2O] %	Corr. [CO_2][2] μg/g	Error (IGL - Raman) μg/g	Total error[3] μg/g
SC02Br3a	1·14E-08	2·4E-12	0·0E + 00	0·77	0	–	–
SC02Br3c	4·74E-07	1·3E-10	2·3E-11	0·78	51	–	–
SC02Br5a	1·04E-07	2·5E-11	1·6E-10	1·39	1602	884	910
SC5Kr1a	3·76E-08	1·5E-11	6·9E-11	1·66	1878	860	886
SC5Kr1b	3·59E-08	3·5E-12	1·5E-11	1·52	787	159	185
SC5k3Gb	1·01E-07	5·7E-11	1·6E-10	2·21	1888	151	177
SC5Kr2a1	1·69E-08	4·4E-12	5·0E-12	1·76	336	–	–
SC5Cr6	3·05E-08	1·4E-11	3·0E-11	2·41	1506	4	30
SC11Dr1_2	2·23E-06	4·2E-09	6·8E-09	3·08	3407	–	–
SC11Dr1d	3·72E-08	3·4E-11	8·7E-11	2·11	2631	–	–
SC11Dr1g	5·02E-09	6·4E-12	1·4E-11	2·37	3024	–	–
SC11Dr1h	7·31E-09	9·0E-12	1·5E-11	2·13	2344	–	–
SC11Dr1i	4·10E-09	5·6E-12	1·5E-11	2·18	4101	–	–

H_2O–CO_2 mass (grams) in the bubble are calculated with Raman spectroscopy (Raman) and Ideal Gas Law method (IGL). Volatile contents are obtained with NanoSims.
[1]Italic underlined numbers are chosen from mass CO_2 bubble (Raman), because it is superior to IGL. SC02Br5a and SC5Kr1a were treated with IGL in Robidoux (2016).
[2]Red colour number is when error is higher than the value itself or IGL is not compared with Raman spectroscopic method.
[3]Adding ±26 μg/g uncertainty from Robidoux (2016) (volume error for 1 pixel/1 μm imprecision for Raman picture treated with ImageJ software + decimal from wavelength cm^{-1}.
Δ, Fermi Diad in Fityk software.

To reconstruct a chronological order of trapping for an MI population ($A_{1–2–3\text{-}etc.}$), the relative distribution of MIs in the crystal growth zones was considered; i.e. one clustered assemblage of MIs in the olivine core can be considered older than an assemblage located closer to the rim (Table 1; Supplementary Data Electronic Appendix 1d and e). A single olivine crystal thus can contain more than 3 chronologically distinct MI populations. For studying the volatile contents of juvenile magmas, however, all 31 MIs selected for Raman spectroscopy were primary inclusions of first order (A_1) with <10 vol. % vapour bubbles (with exception of SC5Dr1c1).

The systematic characterization of olivine crystals and their inclusions in each layer showed distinct textural characteristics (Table 1; Supplementary Data Electronic Appendix 5). Analysed olivine crystals correspond to: G1: No inclusions, G2: Glassy MI (primary), G3: Homogeneous <10 vol. % vapour bubble, G4: Heterogeneous with <10 vol. % vapour bubble + visible oxide, G5: all crystallized + dominant solid phase (oxide), G6: others. Further classification was also made with: A: dominant solid oxide phase, R: reentrant, B: Heterogeneous oxide/vapour.

When selected for Raman spectroscopic analyses, olivines with glass inclusions in each layer were classified in different MI populations (MI with bubble A_B, with bubble and/or oxide A_H, with daughter crystal and/or crystallized border A_X; reentrant characteristics A_R). Primary inclusions without those characteristics were the most favorable samples for measuring volatile contents of the juvenile parental magma, but they do not represent the unique conditions during crystal growth and melt entrapment (Supplementary Data Electronic Appendix 1).

According to the bubble vol. % data illustrated in Supplementary Data Electronic Appendix 1 and reported in Electronic Appendix 3 (e.g. Robidoux *et al.*,

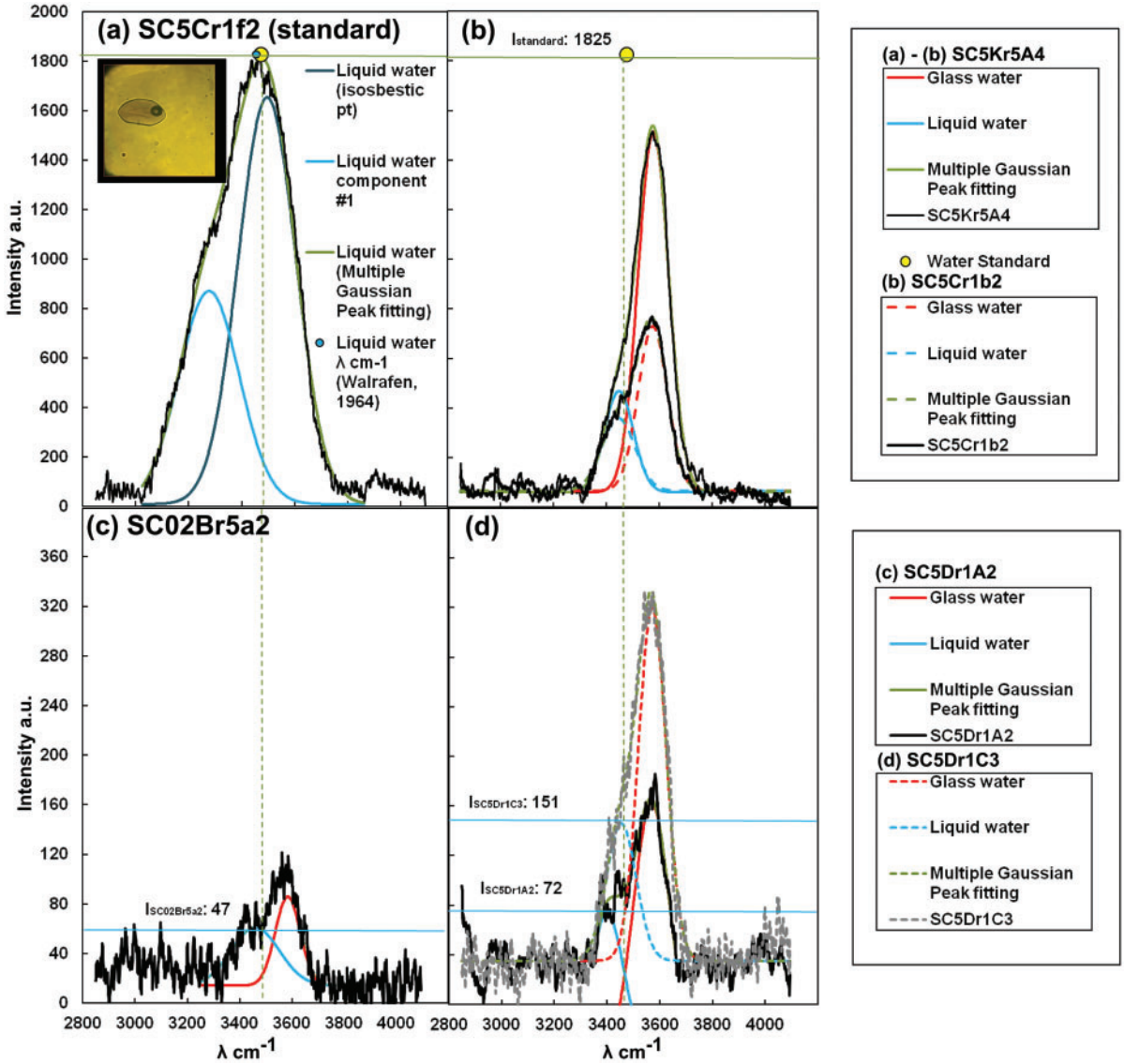

Fig. 6. Raman water spectrum. Liquid- and glass-water Raman spectra collected in bubbles from several MIs. (a) Standard liquid-water band in sample SC5Cr1f2; (b) water bands in samples SC5Kr5A4 and SC5Cr1b2 (see legend to the right); (c) water bands in sample SC02Br5a2; (d) water bands in samples SC5Dr1A2 and SC5Dr1C3 (see legend to the right).

2017), with the exception of SC5Dr1c (13.1 vol. %), the MI populations observed in this study contained similar volume proportions of bubbles, indicating isochoric systems (Roedder, 1984). Bubble-free MIs (Fig. 4) had extremely variable volatile, major element and forsterite (Fo %) contents, whereas bubble-bearing inclusions with smaller proportions of bubbles relative to inclusion volumes (<5 vol. % bubble) had generally smaller contents of water (H_2O wt %). In Fig. 4, MIs having larger bubbles (>5 vol. %) represent H_2O–CO_2–rich mafic magmas with higher olivine forsterite contents and lower SiO_2 concentrations (basaltic composition for most), whereas MIs having smaller bubbles (<5 vol. %) represent slightly more differentiated magmas (basaltic andesite composition).

Within the same MI population, bubble-bearing inclusions of known composition (determined by EMPA and nano-SIMS) had similar textural features; e.g. similar colours and morphologies were encountered at the core of olivine crystals. In comparison, MIs observed at the rims of olivines were characterized by angular shapes and honey-brown colours with dark bubbles. Those MIs did not correspond to the typical morphologies for compositional studies. For example, the G4 MI population was identified in this category (heterogeneous with <10 vol. % vapour bubble + visible oxide), which is generally composed of large MIs (>20 μm) with honey-light brown colour of the glass (Electronic Appendix 1; A_H, A_X, A_R).

To verify any similarities between the inclusion textural characteristics, three categories of MI are illustrated in Fig. 4 and their chemistries are compared. One MI population was chosen for this comparison based on petrographic arguments only (assemblage order

Table 4: Liquid and glass water peak attribution of Raman signal in bubbles

Sample no.	Liquid Water (cm^{-1})	Peak Intensity (I) (a.u.)	Glass Water (cm^{-1})	Peak Intensity (I) (a.u.)	Intensity Ratio: Bubble Water/ Standard Water	Intensity Ratio: Bubble Water/ Glass Water	r^2	σ Intensity (I) (a.u.)	σ Wavelength (λ, cm^{-1})
SC5Dr1c2 (center)	3437	76	3575	203	0·041	0·372	0·971	6·08	4·64
SC5Dr1c3 (border)	3454	111	3572	284	0·061	0·389	0·871	15·60	12·77
SC5Cr1b2	3445	293	3575	663	0·160	0·442	0·986	4·74	3·89
SC5Kr5a3 (center)	3428	91	3571	278	0·050	0·328	0·986	1·90	3·08
SC5Kr5a4 (border)	3447	408	3577	1453	0·223	0·281	0·994	3·36	2·68
SC5Dr1a2	3400	116	3569	205	0·063	0·566	0·921	9·43	6·73
SC5Cr4a2	3412	184	3565	456	0·101	0·405	0·980	3·06	1·88
SC02Br5a2	3460	47	3584	72	0·026	0·651	0·894	22·92	16·60
SC5Cr1f2 (standard)	3474	1826	–	–	1	–	–	59·49	167·31

OriginPro8 software was used to treat background noise and attribute the water peak signal intensities (I) (a.u.) and centered wavelength value (cm^{-1}) with correlation coefficient r^2 and 1σ errors.

A1). None of the bubble-bearing MIs contained oxides, and they were located at the core of olivine crystals. The data set from Robidoux *et al.* (2017) is used for comparison in Fig. 4e–h, and a bubble size limit of 5 vol. % applied to identify real shrinkage bubbles (Lowenstern, 1994). The geochemical parameter values indicate that for most of the layers (Fig. 4e), the sample groups with compositions corresponding to mafic endmembers (SC5C-D and SC11) also represent shrinkage bubbles with >5 vol. %. This tendency is observed for groups contained in olivine with high forsterite contents in basalts (Fig. 4f and h). Olivines with MI compositions corrected for PEC do not show correlation between the percentage of olivine added and inclusion categories (Fig. 4g; shrinkage bubbles, >5 vol. % bubble MIs, and inclusion-free bubbles). The group of bubble-bearing MI's with olivine hosts rich in MgO (high Fo %) follows the typical shrinkage bubble content of 5 vol. %, whereas olivine crystals having lower Fo % contain MIs with high vol. % bubble proportions.

Raman microspectroscopy study

The results of Raman microspectroscopy analyses are presented in this section for each gaseous, liquid and solid phase contained in MIs (n = 31). The position of spectral bands and determination of peak intensities by fitting Gaussian/Lorentzian curves to the Raman spectra are summarized in Tables 2 and 5.

CO_2 densities

Only ten of the analysed bubbles withinf glass inclusions in several olivine crystals showed a clear quantifiable Fermi doublet and proved that CO_2 is present in the shrinkage bubble at ambient temperature. The failure to measure the Fermi doublet in the bubbles in many MIs does not exclude presence of CO_2 in the bubbles, since several factors can contribute to the absence of a reliable Raman signal, including a low CO_2 density, the small dimension of the bubbles, and the depth of location of MIs inside the analysed crystal (e.g. >20 μm; Frezzotti *et al.*, 2012).

CO_2 densities were calculated based on the distance between the two Fermi diads, crosschecking different Raman densimeter equations. Results are summarized in Table 2. The Fall *et al.* (2011) equation calculates densities from 0·171 to 0·342 g/cm^3 (standard deviation SD = 0.05 g/cm^3) and overall shows an error of 0·035 cm^{-1} in the Fermi diad splitting measurements. Those density results are generally from 9–11% higher than those obtained applying the Lamadrid *et al.* (2017) linear equation. Yamamoto & Kagi's (2006) densimeter was also tested, but the results diverge (0·161–0·361; SD = 0·07 g/cm^3). Other commonly used densimeter equations (e.g. Kawakami *et al.*, 2003; Song *et al.*, 2009) were not considered, since they are generally applied to high-density CO_2 inclusions (cf., Lamadrid *et al.*, 2017).

For the series SC02B and SC5K, the Fall *et al.* (2011) densimeter showed a narrow interval of CO_2 densities for three samples (0·292–0·300 g/cm^3). From those density measurements and calculated bubble volumes, the highest derived CO_2 mass ($4{\cdot}36 \times 10^{-10}$ g) was found in inclusion SC02Br5a, which has a bubble larger in size compared to most MIs observed in olivine grains from the same series (3·12 x10^{-8} cm^3). Within the series SC5C, one olivine crystal had four out of five MIs with a bubble that could be used to calculate Δ, resulting in a wide range of CO_2 densities (0·171–0·292 g/cm^3). Overall, the CO_2 mass ranges between 1·46 x10^{-11} to 6·94 x10^{-12} g. In the SC5D series, two olivine crystals had three out of five MIs with bubbles having measurable Δs and their densities are the highest among all our samples (0·310 g/cm^3). The highest CO_2 mass was found in this series of samples, for bubble SC5Dr3a1 (4·89x10^{-10} g), which is a bubble larger compared to most samples in this study (3·67x10^{-8} cm^3). In SC11D, uncertainties remain concerning the presence of CO_2, since no Fermi diad peaks were observed during the Raman analysis.

H_2O

In only one MI (SC5Cr1f2) the bubble clearly showed a Raman spectrum corresponding to liquid water,

Table 5: Mineral identification with Raman spectroscopy

SAMPLES	Carbonate	Sulphate	Pyrite	Marcasite	Chalcopyrite	Magnetite	Water	CO_2	FWHM
SC02B									
SC02Br3a1				x	x				
SC02Br3b1									
SC02Br3c1			x?	x					
SC02Br3d1									
SC02Br3e1			x		x(?)			x	
SC02Br3f1					x				
SC02Br3g1					x				
SC02Br3h1					x				
SC02Br5a1							x	x	
SC5k									
SC5KR3A1	x	x			x(?)	x(?)			19.8
SC5KR3B1		x				x(?)			
SC5kr5a1			x		x		x	x	
SC5D									
SC5Dr1a1	x				x		x	x	13.1
SC5Dr1b1	x							x	16.4
SC5Dr1c1	x			x	x		x	x(?)	18.8
SC5Dr3a1				x	x			x	
SC5Dr3b1	x(?)			x	x			x(?)	19.7
SC5C									
SC5Cr1a1	x				x			x	24.6
SC5Cr1b1	x						x	x	16.4
SC5Cr1c1	x		x		x			x	29.5
SC5Cr1d1	x				x				16.4
SC5Cr1e1	x				x			x	22.9
SC5Cr1f1	x				x		x	x(?)	19.7
SC5Cr4a1	x				x		x	x(?)	24.6
SC5Cr4b1	x				x			x	24.6
SC5Cr4c1	x(?)							x	34.4
SC11D									
SC11Dr1a1	x				x				16.4
SC11Dr1b1	x				x				9.8
SC11Dr1c1									
SC11Dr1d1	x*				x				8.2
SC11Dr4a1					x				

Mineral identification are confirmed with x symbol after background noise signal is treated and mineral intensity peaks are confirmed with Fityk 0.9.8 free software. When a sample is marked with an x(?), it means a noisy spectrum background and low peak intensity makes the identification difficult and x* stands for stable/crystalline magnesite signal.

represented by an isosbestic point of 3474 cm^{-1} (3460 $\pm$ 60 cm^{-1}; Walrafen, 1964, 1967). In San Cristóbal samples, the recorded positions for liquid water vary between 3400 and 3474 cm^{-1}. Numerous overlapping bands are observed in most shrinkage bubbles, which result from additional vibrations arising from O–H groups in hydroxyls and H_2O molecules in the glass. The O–H vibrations in the glass water have a spectrum centered at 3565–3577 cm^{-1} within the range of wavelengths for different glass compositions (3100–3750 cm^{-1}) reported by Thomas *et al.* (2006). Fitting of overlapping O–H bands, performed by applying the multiple-peaks fitting function in OriginPro8 software is presented in Fig. 6, with each liquid water peak exceeding the signal background and the bands from the O–H groups in glass water. The liquid water peak with the highest intensity (1825 a.u. at ~3474 cm^{-1}, SD = 6 cm^{-1}) was used as a reference standard (Fig. 6a).

Based on the statistical treatment of spectra, the presence of liquid H_2O was confirmed in seven shrinkage bubbles (Fig. 6b–d). The peak intensities appeared to be higher if spectra were collected at the bubble–glass interface (SC02Br5a2, SC5Dr1c2, SC5Dr1c3, SC5Kr5a3, and SC5Kr5a4; Supplementary Data Electronic Appendix 1, Table 4). In all cases, liquid H_2O coexists with CO_2 (Table 5). After using a polynomial function for two Gaussian peaks (liquid water and glass water), the σ intensity was below 23 a.u., and the σ wavelength was below 16·6 cm^{-1}, indicating that the peak-fitting method is generally well suited for the two polynomial Gaussian functions.

(Daughter) mineral phases

Several mineral phase associations (size $\leq$ 1 μm) are present within bubbles (Fig. 7; Table 5). The most common mineral phase is magnesite (Fig. 7c and d), detected in 17 out of 31 bubbles, seven of which in the presence of CO_2 and 5 with both $H_2O + CO_2$ (Table 5). The main carbonate peaks are registered in the intervals from 1094–1090, and 330–314 cm^{-1}, showing variable downshifting for the different vibrations. In magnesite

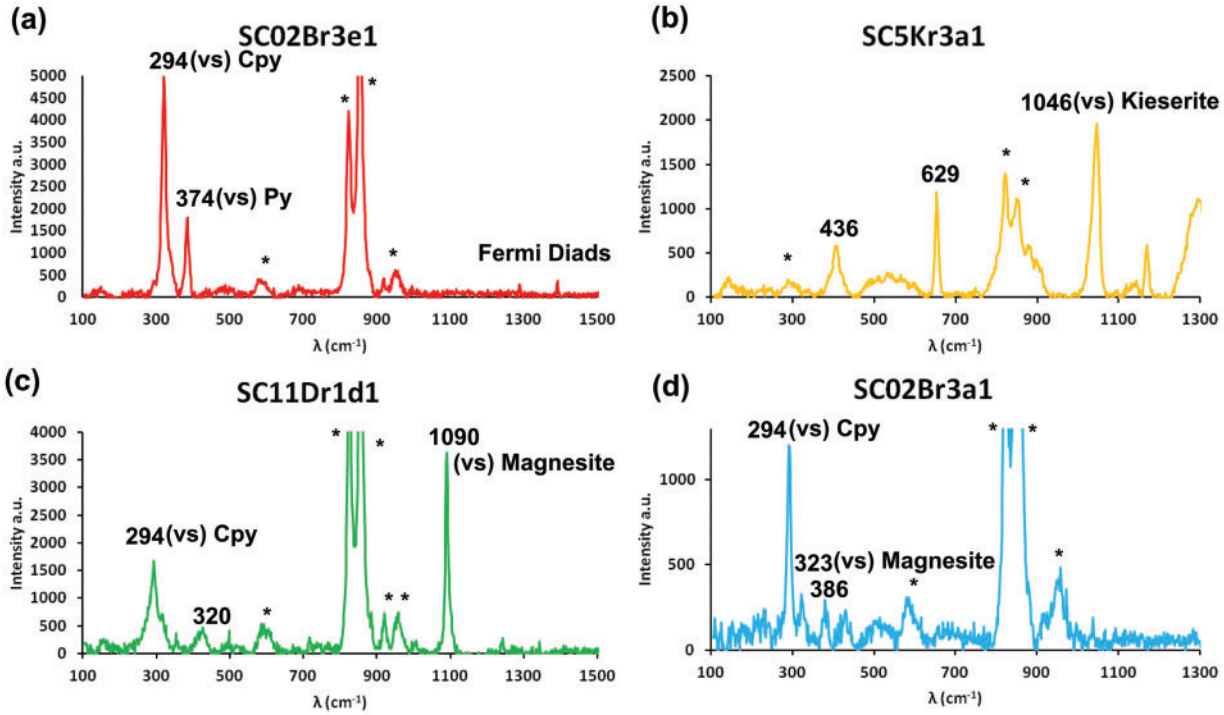

Fig. 7. Raman mineral identification in bubbles. Attribution of Raman main vibrations «vs» of mineral phases present inside bubbles. Asterisks (*) represent peaks from the olivine host. (a) sample SC02Br3e1; (b) sample SC5Kr1; (c) sample SC11Dr1d1; (d) sample SC02Br3a1.

($MgCO_3$), downshifting of the main carbonate peaks is indicative of Fe substitution (e.g. Boulard *et al.*, 2012), suggesting a composition from pure magnesite to Fe-bearing magnesite. The full width at half maximum height (FWHM) of the main carbonate peak at 1090–1094 cm^{-1} is also variable, and ranges between 8.2 and 29.5 cm^{-1} indicating variable degrees of crystallinity. Those magnesite crystals having FWHM in the main carbonate band at $>20\,cm^{-1}$ are interpreted as (low-temperature) 'amorphous Mg-carbonates'. Sulfides coexisting with CO_2 (12/23 inclusions), H_2O (5/23) and/or magnesite (14/23) include chalcopyrite (22/31), marcasite (5/31), and pyrite (3/31). A hydrous sulfate, of kieserite type ($MgSO_4 \bullet H_2O$), coexists with sulfides in two bubbles (Fig. 7a and b).

DISCUSSION

Raman spectra and SEM analyses in naturally cooled bubbles inside MIs in olivine indicate the presence of a complex C–O–H–S fluid system, as revealed by the associations between liquid water, carbon dioxide, carbonates, sulfides and hydrous sulfates at ambient temperature. These findings are consistent with those of Esposito *et al.* (2016 and references therein) who first reported the presence of liquid water, native sulfur and sulfates in shrinkage bubbles inside reheated and quenched MIs in olivines from Mount Somma-Vesuvius. Considering that the San Cristóbal MIs were not reheated in the laboratory, they can be used to characterize the natural evolution of C–O–H–S-rich fluids in shrinkage bubbles during the natural cooling that follows an eruption. In the following section, the presence of distinct volatile species is discussed in comparison with their respective roles in magmatic and hydrothermal processes. A conceptual model of shrinkage-bubble evolution during cooling is also presented to explain the presence of precipitated minerals. The observed paragenetic mineral association is finally compared with magmatic hydrothermal mineralization analogs frequently investigated in models of volcanic-related copper deposits.

Raman-calculated C-O-H fluid compositions

Inside the bubbles, the CO_2 Raman-calculated density varied from 0·171 to 0·310 g/cm^3 with derived masses between $1{\cdot}4 \times 10^{-11}$ and $6{\cdot}8 \times 10^{-9}$ g. The re-estimated bulk CO_2 mass in the inclusion varied between 2·23 and $4{\cdot}10 \times 10^{-9}$ g. In total, between 39% and 68% of the CO_2 estimated mass had been lost from the original MI to the shrinkage bubble. In SC11D inclusions, where CO_2 Fermi diads were not detected during the Raman analysis, the processing steps of the IGL method calculated 29–42% CO_2 loss (Table 3). In the IGL method, the bubble environment is considered as an ideal closed vapour H_2O–CO_2 system, where volatiles have already diffused from the glass to the shrinkage bubble during cooling. Based on this assumption, the mass of CO_2 within inclusion bubbles can be converted into the number of moles estimated using the IGL method

(PV = nRT) (Robidoux, 2016). Considering only corrected CO_2 contents validated by both IGL and Raman spectroscopy data, these values were 3- to 15-fold higher in inclusions with shrinkage bubbles compared to bubble-free inclusions. Such a difference would be dramatic when estimating the entire dissolved magmatic CO_2 budget of individual eruptive events. For example, the maximum CO_2 mass budget for the San Cristóbal eruption of 1976 would be of about 8550 tons if Raman-corrected inclusions with a shrinkage bubble were found in 100% of the olivine crystals. In contrast, glass inclusions (with or without a shrinkage bubble) that are not corrected represent a minimum CO_2 budget of 350 tons (Supplementary Data Electronic Appendix 4; Robidoux *et al.*, 2015*a*).

In melt inclusions, the formation of shrinkage bubbles (Lowenstern, 2015 and references therein) is well known to affect CO_2 diffusion, but this process is insufficient to explain the significant loss of CO_2 at San Cristóbal in all populations of inclusions. A significant CO_2 loss was also found in MIs analysed by Robidoux *et al.* (2017), where bubble-free inclusions (17–406 μg/g in 20 of the 41 samples) do not even match the IGL and/or the Raman-corrected CO_2 contents of bubble-bearing inclusions (718–1889 μg/g in five of the 41 samples). Neither do they exceed their uncorrected original contents (<71–527 μg/g CO_2) (Fig. 8a). This means that for a large number of inclusions, independent of textural characteristics and population, CO_2 was already lost to the vapour phase and escaped the magma reservoir before entrapping processes occurred (Métrich & Wallace, 2008). This is clearly supported by the clear differences in lost H_2O, CO_2, S, and Cl (>26%, >60%, >34% and >11%, respectively) between basaltic and basaltic andesitic MIs with shrinkage bubbles. This latter result demonstrates that during fractional crystallization, pre-entrapment processes already control the most substantial proportion of volatile loss.

The values obtained using the model with the IGL-corrected CO_2 mass did not always match those calculated from Raman densimeters. However, the small number of Raman analyses that matched nano-SIMS data for the same inclusions made it impossible to provide a definitive explanation based on quantitative evaluation of data reproducibility, at least for volatile contents from nano-SIMS analysis (e.g. Aster *et al.*, 2016). Other than methodological considerations, inconsistencies in calculated CO_2 masses (Table 3) could be due to several natural processes: (1) part of the carbon dioxide reacted to form carbonates along the bubble walls at sub-magmatic temperatures, lowering CO_2 density (e.g. Kamenetsky, 2001, 2002, 2007); (2) the fluid chemistry of each bubble environment is more complex than an ideal CO_2-H_2O gas mixture as modeled by IGL. The latter process is supported by the presence of sulfur (e.g. sulfides and sulfates in bubbles; Fig. 7, Table 5) that may additionally affect the modeled mass fraction of each volatile species in the vapour–fluid mixture (Fig. 8). Sulfur is undoubtedly an additional essential constituent migrating from the melt (see the previous section and Esposito *et al.*, 2016).

Liquid water inside the shrinkage bubble and MI water loss

Liquid water Raman peaks are present at the bubble–glass interface of natural glass inclusions at ambient temperatures, which supports water being present inside the bubble (Lowenstern *et al.*, 1991; Yang & Scott, 1996; Kamenetsky *et al.*, 2001, 2002; Robidoux *et al.*, 2015*b*; Esposito *et al.*, 2016). Liquid water peaks were detected in seven bubbles (Table 4), and their intensities appeared to be higher if spectra were collected at the bubble–glass interface (SC02Br5a2, SC5Dr1c2, SC5Dr1c3, SC5Kr5a3, and SC5Kr5a4; Supplementary Data Electronic Appendix 1, Table 4). It is possible that the thin film of liquid water present at the bubble–glass interface results from H_2O–CO_2 immiscibility from a high-temperature homogeneous C–O–H fluid on cooling. However, many uncertainties remain regarding the size of the water annulus inside the bubble, since it cannot be visualized using the available analytical instruments (Esposito *et al.*, 2016).

The mass of water present in the seven investigated bubbles represents only 0·5–3·0% of the total water mass in the glass (Table 3). These observations suggest that a water content ranging from only <0·1% to 0·3% could have been reintroduced into the MIs of San Cristóbal by the IGL method (Table 3). This is a particularly small amount of water for any bubble that may be formed by PEC (Steele-MacInnis *et al.*, 2011) and is not relevant compared to the panoply of known physicochemical processes inducing water loss from the glass (cf., Roedder, 1984; Qin *et al.*, 1992; Danyushevsky *et al.*, 2002; Baker *et al.*, 2005; Zhang, 2010; Chen *et al.*, 2011; Gaetani *et al.*, 2012; Bucholz *et al.*, 2013; Hartley *et al.*, 2015 and references therein). For naturally cooled and quenched inclusions containing a shrinkage bubble, the decreasing internal pressure along with dehydration during cooling may explain some of the substantial water loss (Fig. 9a, b, and d). This alternative explanation to the process of water loss is supported by experimental rehydrated and homogenized MIs (Sobolev & Danyushevsky, 1994). The H_2O–CO_2 correlation and the dependence on bubble expansion reflect the internal pressure inside the silicate melt increasing with hydration of the inclusion (e.g. Mironov *et al.*, 2015).

The above considerations indicate that the problem of the low water content of MIs is not resolved for San Cristóbal, because the naturally quenched MIs could represent partially trapped degassed melts. MIs could even be affected by deep-to-shallow carbon dioxide fluxing in the plumbing system (Blundy *et al.*, 2010), considering the high CO_2/S values measured at the central crater, but some uncertainties remain regarding the dispersion of the volatile data from the MIs, as illustrated in Fig. 8a and b (Aiuppa *et al.*, 2014; Robidoux *et al.*, 2017). Correction factors are, therefore,

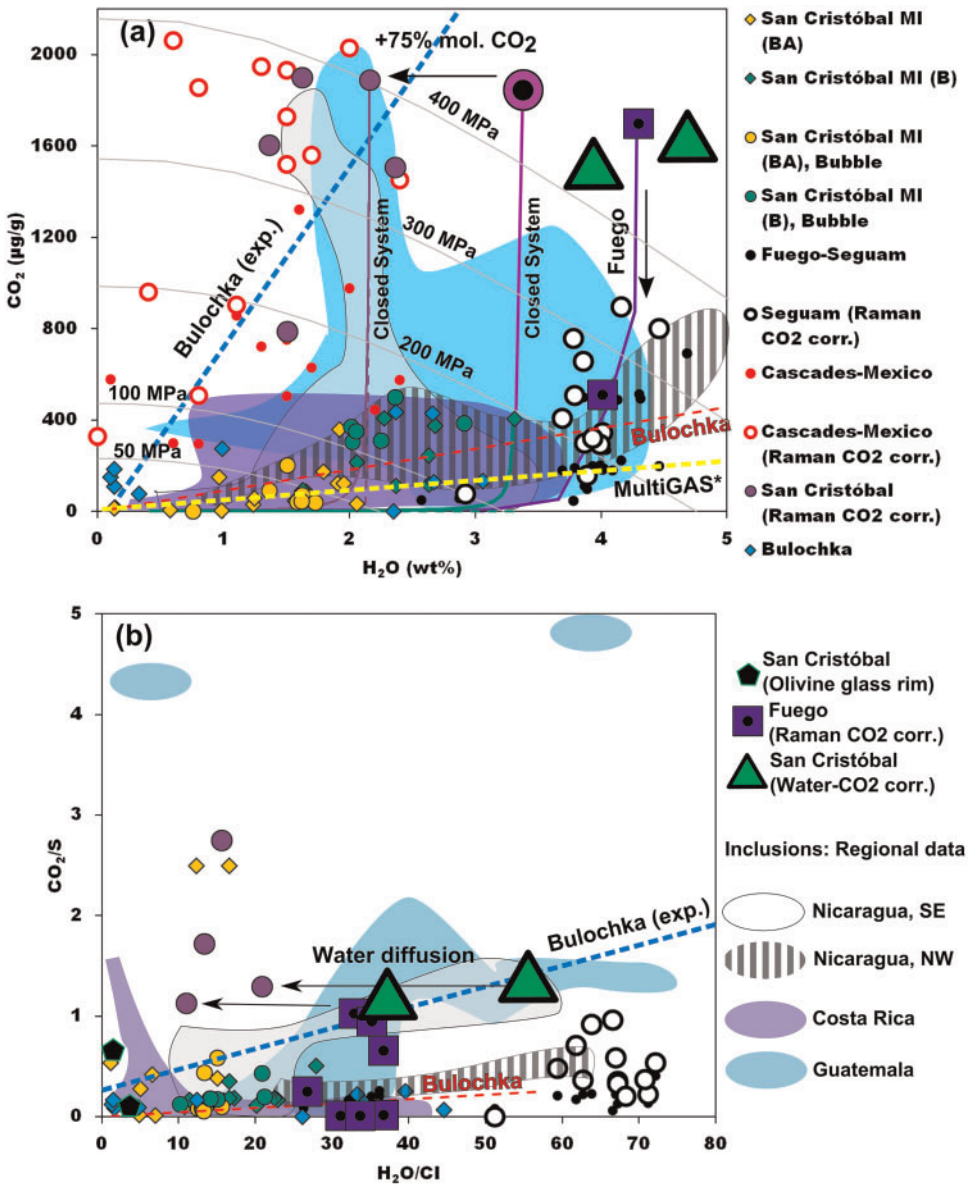

Fig. 8. Major volatiles measured in melt inclusions from olivines sampled at typical subduction zone volcanoes and corrected for their CO_2 content. San Cristóbal melt inclusions are illustrated with B for basalt (green), BA for basaltic andesite (orange) with lozenges for MIs without bubbles and circle symbols for MIs with bubbles. Corrected-Raman samples for CO_2 budgets from San Cristóbal are represented by purple dots, including the most primitive sample (large purple circle with centered black dot). Green triangles for water diffusion correction are illustrated, including the closed system degassing path (calculated with the Solex model; Witham *et al.*, 2012). The values are corrected with H_2O/K_2O proxies listed in Supplementary Data Electronic Appendix 3. Fuego-Seguam samples are from Moore *et al.* (2015), including white circles representing corrected-Raman samples for CO_2 budgets at Seguam and blue squares with centered black dots at Fuego (single black dots are for uncorrected values). Cascades-Mexico samples are from Aster *et al.* (2016) including Basalt of Round Valley Butte and Basalt of Old Railroad Grade scoria cones in the Cascades and Jorullo with Parícutin from the Trans-Mexican Volcanic Belt. Heated Bulochka inclusions with bubbles from scoria cone in Mironov & Portnyagin (2011) are illustrated with their linear trends (red dashed line), because their homologous uncorrected CO_2 MIs have similar volatile degassing trends to San Cristóbal. The experimental heated/hydrated inclusions with bubbles from the Mironov *et al.* (2015) linear trend are illustrated with a blue dashed line. MultiGAS* data are illustrated with a yellow dashed line (Aiuppa *et al.*, 2014; Robidoux *et al.*, 2017). (a) CO_2 vs H_2O; isobars are from Robidoux *et al.* (2017); (b) CO_2/S vs H_2O/Cl.

necessary, but they do not produce an accurate calculated water content for inclusions from San Cristóbal (Fig. 8). By using the highest H_2O/K_2O values of the most primitive inclusions (Sadofsky *et al.*, 2008; Johnson *et al.*, 2010; Aster *et al.*, 2016), the relative water content lost by pure degassing (Supplementary Data Electronic Appendix 3), induced crystallization, carbon dioxide fluxes, or H^+ diffusion can be accurately quantified at San Cristóbal. For example, the most mafic and volatile-rich inclusion without a shrinkage bubble (SC11D1a; $H_2O/K_2O = 9$) had an excessive water content (>9·0 wt %), while for the least-differentiated MI with a shrinkage bubble (SC11Dr1i; $H_2O/K_2O = 5{\cdot}5$) the water content shifted from initially Raman-corrected

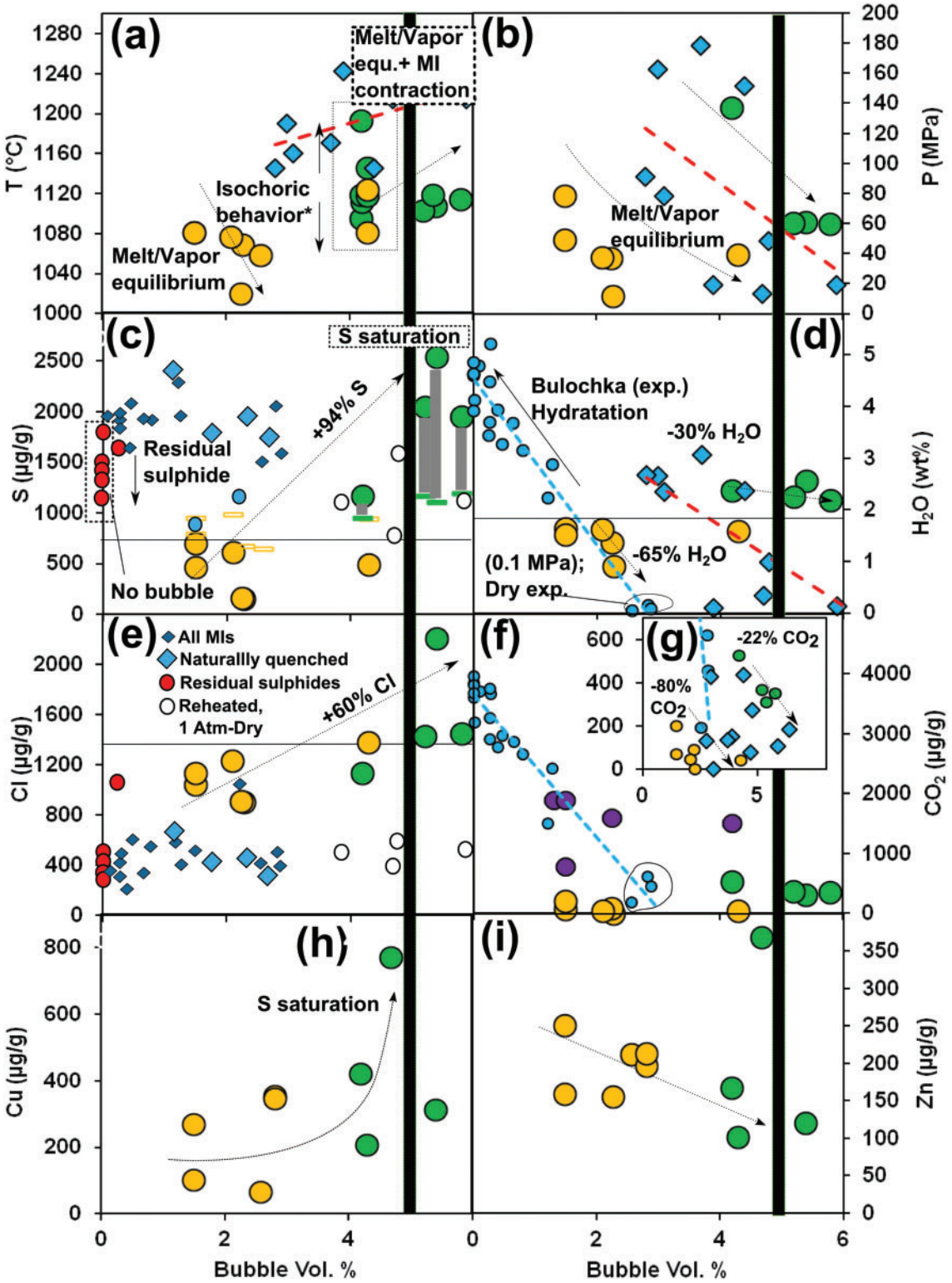

Fig. 9. Intensive parameters as a function of relative bubble/inclusion volume. Black horizontal lines in c,d,e are demarking the arbitrarily chosen percentage difference (%) between basalt and basalt andesite richest in volatile contents. The broad black vertical line crossing all figures (except Fig. 9g) shows the maximum arbitrarily chosen 5 vol. % typical shrinkage bubbles (Lowenstern, 1994). (a) Temperature, (b) pressure, (c) sulfur, S-saturation with green (basalt) and orange (basaltic andesite) coloured horizontal bars representing the estimated sulfur content (µg/g) for sulfur undersaturated primitive magmas calculated using the equation of Fortin *et al.* (2015). (Note: none of the basalt andesites are S-saturated, but basalt MIs samples SC5Cr6, SC11Dr1d-g-h-I are S-saturated.) Grey vertical bars show the estimated sulfur excess (µg/g) from natural melt inclusions and possible residual sulfide (Electronic Appendix 3, 4), (d) Water, Mironov *et al.* (2015) experimental data on Bulochka volcano with arrow pointing in the direction of experimental heating, (e) Chlorine, with most data within analytical errors (no correlation, but 60% diffusion between minimum and maximum values), (f) Carbon dioxide (0–5000 µg/g), with CO_2 corrected-Raman samples represented by purple circles, (g) Carbon dioxide (0–700 µg/g), (h) Copper, (i) Zinc. See also legend in Fig. 8.

CO_2 MIs to 2·2–5·5 wt % H_2O, which is consistent with typical volcanic arc magma water contents ($n = 3$; Fig. 8a and b; Plank *et al.*, 2013 and references therein). Only part of the corrected water budgets thus conform with degassing trends in several CAVA samples, including similar open-vent degassing/active stratovolcanoes that were also corrected for CO_2, such as Fuego (Moore *et al.*, 2015).

Consequently, in a classic diagram of CO_2 vs H_2O (Fig. 8a), applying solubility models with the uncorrected water content (2·1 wt % H_2O) but Raman-corrected MIs for CO_2 (SC5k3Gb; 1889 μg/g) artificially shifted the degassing paths to >75 mol % CO_2 from the ideal path initiated by the most-primitive MI (SC11D1a; 3·3 wt % H_2O; Robidoux *et al.*, 2017). If this trend is realistic, the Raman-corrected samples for CO_2 at San Cristóbal in Fig. 8a linearly follow the experimental data for MIs from Bulochka tephra, where bubbles undergo high-temperature dehydration (Mironov *et al.*, 2015) (e.g. Fig. 10d). In multiple volatile plots (CO_2/S vs H_2O/Cl; Fig. 8b), a high degree of scattering of Raman-corrected CO_2 values is observed outside of the typical compositional fields of CAVA MIs (Robidoux *et al.*, 2017). Of these data, two water-corrected values (triangles in Fig. 8) were consistent with other compositional fields from the volcanic arc despite uncertainties about the amount of water lost by diffusion. In addition, the major volatile contents from uncorrected bubble-bearing inclusions overlap with values from bubble-free inclusions. This means that CO_2 corrections are incomplete without taking into account all H_2O–S–Cl corrections, and particularly H^+ diffusion (Fig. 8a and b).

It could be argued that San Cristóbal MIs with Raman-corrected CO_2 values should be considered as a group of inclusions trapped under different conditions. However, those bubble-bearing inclusions were observed in the same MI population together with bubble-free inclusions (Table 1; Supplementary Data Electronic Appendix 1; Fig. 4). This is particularly important given that some doubts persist about why H^+ diffusion affects some MIs, but not others in the same group of MIs in the core of a single olivine (Danyushevsky *et al.*, 2002). From data sets compiled with bubble-free MI in Robidoux *et al.* (2017) by comparing shrinkage bubbles of inclusions classified into the same group (three pairs of comparable MIs), for the small amount of chemical data available (Supplementary Data Electronic Appendix 3), the water content vs bubble diameter parameters are very similar in each MI population (except for the different bubble sizes of SC5Kr1a and SC5Kr1b). However, there is a general tendency for higher H^+ diffusion (lower water content) in smaller shrinkage bubbles, and similarly, although to a lesser extent, in larger inclusions in comparison with bubble-free MI (e.g. Fig. 4a; Supplementary Data Electronic Appendix 3). Because only oxide-free MIs located at the core of olivine phenocrysts were analysed, the present results do not provide evidence that H^+ diffusion or PEC (% Ol added) change within the same MI population. Instead, according to chemical parameters and bubble vol. %, melt compositions vary between MIs in different crystals, and there are correlations with the shrinkage bubble, inclusion size, morphology, and water content (Fig. 4). One hypothesis is that the contact surface area of the bubble–glass interface plays a role by enhancing diffusion effects during bubble formation and later PEC effects.

A new model for the formation of a shrinkage bubble

The complex association of fluid and solid phases detected in melt inclusion bubbles suggests that two central questions need to be addressed when considering the mechanisms underlying the nature of fluids trapped inside a shrinkage bubble (Fig. 11): (1) Is the shrinkage bubble dominated by carbon dioxide and progressively filled by other volatiles via diffusion processes, leading to C–O–H–S fluid–glass interactions (Fig. 11a)? (2) Does a shrinkage bubble result from both melt contraction and the exsolution of C–O–H–S volatiles due to the decrease in pressure after melt droplets are trapped as inclusions (Fig. 11b)?

One way to determine the mechanisms underlying bubble formation at San Cristóbal is to evaluate the relationships between intensive primary thermodynamic properties from the inclusion and the relative bubble/inclusion volume ratio (Figs 4 and 9). Those intensive variables are the crystallization temperature (i.e. MI trapping), the pressure, composition of volatiles and the concentration of major elements in the silicate melt (Fig. 4), which can all be derived from nano-SIMS and EMP analysis of glass inclusions. The first distinctive observation comes from the water content at San Cristóbal that decreases linearly with the relative bubble/inclusion volume (Fig. 9d), previously described as a dehydration effect during the natural cooling of MIs (Mironov *et al.*, 2015). A particularly interesting observation is that MIs containing a pure shrinkage bubble (in five of ten samples) closely follow an inverse isothermal hydration trend (1150–1200°C) (Figs 8a, b, and 9d), except for bubbles with sizes >4 vol. % (mostly basalts; in the other five samples). Bubble-bearing inclusions that respect those conditions also have basaltic composition and their olivine-hosts have high forsterite contents (Fig. 4e, g, and h). Larger bubble inclusions do not linearly follow the previous trends, so we suspect that they do not conform to the criteria for classification as pure shrinkage bubbles (e.g. Lowenstern, 1994). Otherwise, all MI bubbles had vol. % falling within the pure shrinkage bubble categories of the Moore *et al.* (2015) model (supplementary calculator), despite very few correspondences between measurements and theoretical vol. % data and few inclusion samples that have the correct input parameters (Supplementary Data Electronic Appendix 3).

There is a difference in the vol. % of the shrinkage bubble between basaltic and basaltic andesite MIs. There are also distinct carbon dioxide contents lost

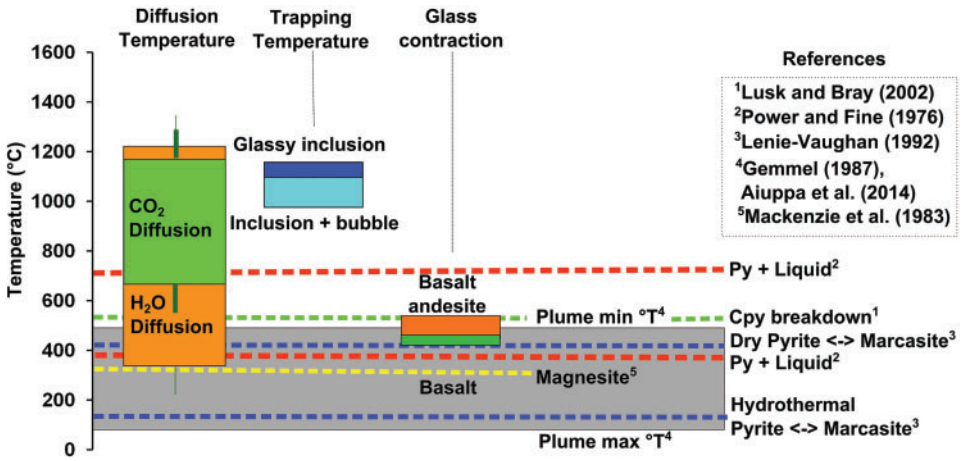

Fig. 10. Temperature proxies of bubble cooling environment in naturally quenched melt inclusions at San Cristóbal. Closure temperatures (Tc) for water diffusion are illustrated with orange rectangles and the respective SD (°C) error bars (including estimated temperatures for their minimum, average and maximum activation energy, using the equation of Zhang & Stolper, 1991). Closure temperatures for CO_2 diffusion are estimated with a modified equation from Watson (1991) as in Robidoux (2016). Glassy inclusions (dark blue rectangle) and MIs with bubble samples (light blue rectangle) from Robidoux *et al.* (2017) are shown with their equilibrium olivine crystallization temperature, assumed as trapping temperature (equation 16 in Putirka, 2008). Glass transition temperatures (glass contraction) calculated in Supplementary Data Electronic Appendix 4 are shown with rectangles for basalts (green) and basaltic andesites (dark orange) (Giordano *et al.*, 2005). Mineral temperature stability intervals (dashed colour lines) and central plume temperatures (grey rectangle) are indicated with their references.

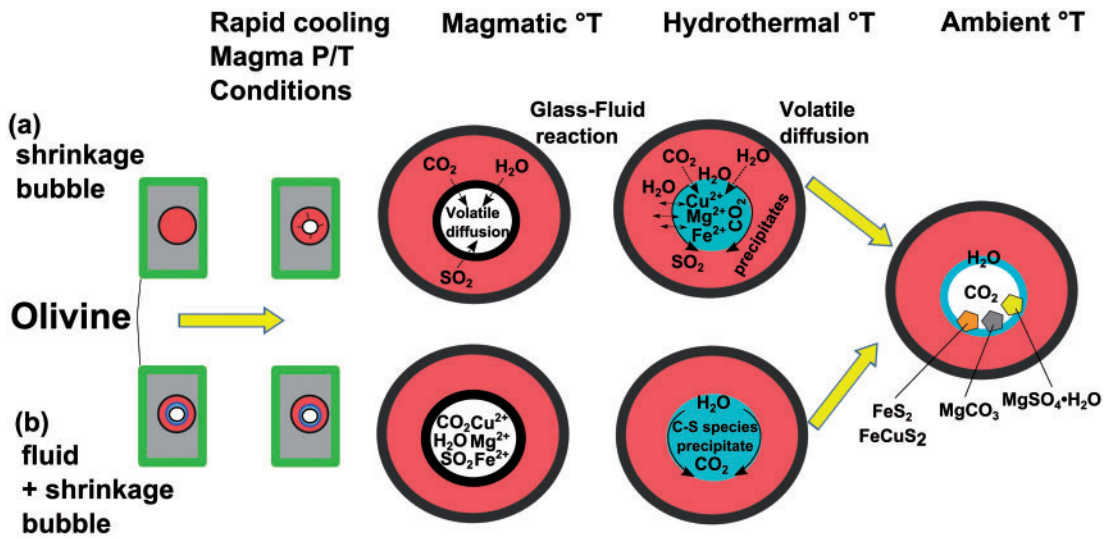

Fig. 11. Models for the evolution of the C–O–H–S magmatic fluid system inside shrinkage bubbles of melt inclusions. (a) Volatile diffusion and glass–fluid reaction in shrinkage bubbles leading to hydrothermal to ambient temperature mineral precipitation; (b) (Immiscible) fluids trapped in shrinkage bubbles leading to hydrothermal to ambient temperature mineral precipitation.

between inclusions of different composition, with basaltic and basaltic andesitic MIs losing 41% and 80% CO_2, respectively (Fig. 9f and g). If the melt–vapour equilibrium is maintained during eruptive cooling (Lowenstern, 1994, 1995), the variations in the volume percentage of the shrinkage bubble may be explained by differences in crystal–melt–host contractions that would induce variable bubble expansion (Riker, 2005; Aster, 2015). We thus suggest that the mechanism underlying bubble expansion can vary depending on melt composition and fluid density (e.g. *P–T* conditions, and rate of post-entrapment cooling (Lowenstern, 1995; Danyushevsky *et al.*, 2002). Fig. 9a and b show that this hypothesis applies particularly well to the smallest shrinkage bubbles of San Cristóbal, but not to those MIs following isochoric trends or approaching the critical bubble proportion of 5 vol. % (Lowenstern, 1994). Otherwise, during eruptive cooling (e.g. Aster *et al.*, 2016), when San Cristóbal MIs reached the glass transition temperature (479–527°C; Fig. 10, Supplementary Data Electronic Appendix 4), bubbles may have expanded slightly for one last time before being

quenched (Anderson & Brown, 1993). During this final process, differences in the extent of bubble expansion depend on the cooling rate (Lowenstern, 1994) and the glass transition temperatures linked to the remaining dissolved water content (Figs 9 and 10) (Giordano *et al.*, 2005). We therefore propose that the bubble volume percentage varies with the magnitude of the difference in the thermal expansivities of the crystal host and melt upon cooling (Roedder, 1979; Lowenstern, 1994, 1995). If doubts remain about whether a bubble is a shrinkage bubble, some other factors may have been involved in their formation. For example, Steele-MacInnis *et al.* (2011) showed that PEC certainly drives the formation of bubbles, because the minerals crystallizing at the wall of the MI will always have a higher density than the trapped melt. In addition, H^+ loss via diffusion can also cause the formation of a bubble (Bucholz *et al.*, 2013), as can melt leaking after MI formation (Lowenstern, 1995). These assumptions are not fully supported by the present dataset, because, for any bubble vol. %, no correlation exists with water content (e.g. water loss with diffusion) and the percentage of olivine added for PEC (Fig. 4f).

Sulfur and chlorine species dissolved in the melt behave differently from the strongly pressure-dependent H_2O–CO_2 pair, as indicated by their contents being enriched by 94 and 60% with the bubble vol. %, respectively. This is partially reflected in the experimental datasets of Mironov *et al.* (2015) (Fig. 9c and e) and implies that the bubble–inclusion interface plays a significant role in the C–O–H–S–Cl chemistry due to bubble–glass interactions. For example, does bubble nucleation act on the silicate melt density by decreasing the pressure-dependent volatile bonds in the silicate melt and favoring higher S–Cl solubility? Also, could larger bubbles increase the surface area in contact for the reaction during natural glass dehydration (Anderson, 1991) and favour condensation of liquid water at low temperatures (Figs 10 and 11)? Correlating the sulfur and chlorine contents is not straightforward based on literature data and the chlorine glass concentration is not modified; that is, it remains within the EMP analytical error. Indeed, basalts may contain residual sulfides, notably when sulfur contents decrease in the melt (e.g. Mironov *et al.*, 2015).

For the case of sulfur, one question is whether the formation of sulfide/sulfate phases inside the bubble depends on the volumetric expansion of bubbles. Sulfides and sulfates are detected in bubbles from different inclusions, and basaltic glass inclusions often show evidence of sulfide precipitation (Table 5). For example, MIs SC11Dr1b and SC11Dr1g in Fig. 9 contained chalcopyrite (Cpy) at the bubble–glass interface, as did 11 bubbles in 14 inclusions of the basaltic series (SC5C and SC11D series). The SEM images in Fig. 3 clearly show the presence of Cpy crystals in bubbles SC5Cr1a, SC5Cr1b, and SC11Dr1g, and also support the hypothesis of sulfide/sulfate precipitation. Those MIs with Cpy inside bubbles also correspond to more significant bubble vol. % where sulfur saturation levels are reached (Fig. 9d). Variations in the sulfur content in bubbles >4·0 vol. % in the natural inclusion system of San Cristóbal correspond to sulfur saturation of basaltic MIs, similar to any other volatiles. We thus suggest that the smaller volume percentage of bubbles in basaltic andesitic MIs having a lower sulfur content may just reflect the decrease of sulfur due to degassing during magma differentiation before MI trapping; during post-entrapment, there is a sufficient amount of sulfur at the bubble–glass interfaces to form sulfide/sulfate minerals at low temperatures, which possibly may reflect residual sulphide precipitation as in Mironov *et al.* (2015) (Fig. 9c).

The above hypotheses, however, do not explain how volatiles migrate into the bubble, and hence further consideration of the mechanisms underlying the formation of vapour bubbles is necessary. The physical models proposed in the literature suggest that a bubble can nucleate due to isochoric cooling of a trapped homogeneous liquid, which later causes depressurization resulting in the exsolution of a low-density fluid phase inside the inclusion (Lowenstern, 1995, 2001) (cf. Figs 4 and 9). At San Cristóbal, this holds well for shrinkage bubbles with variable sizes from 0·9 to 2·8 vol. %; note that typical shrinkage bubbles are 0·2–5·0 vol. % (Lowenstern, 1994). An additional process affecting bubble chemistry is then needed to explain the presence of C–O–H–S fluid and solid phases (Kamenetsky *et al.*, 2001, 2002). Mineral precipitation could be explained by greater hydration of the glass (Lowenstern, 1995) and elemental diffusion when the bubble ceased to expand at the glass transition temperature. The San Cristóbal data could support this dynamic process considering that the pyrite-chalcopyrite precipitation temperature range (500–700°C; Fig. 10) overlaps with glass quenching temperatures (<530°C) (Supplementary Data Electronic Appendix 4).

Two processes (Fig. 11a and b) are plausible at San Cristóbal for explaining the C–O–H–S volatile migration in the inclusions with larger bubble sizes (3·5–7·6 vol. %), which are mostly basaltic (c.f., Figs 4h and 9): (1) fluids fractionated from the trapped melt and (2) the presence of immiscible S-rich liquids. Identifying the right process is critical to understanding how the early Mg-, Fe- and Cu-rich minerals and fluids are formed and isolated inside some inclusions. One way to study this phenomenon is to explore the processes leading to mineral precipitation upon post-entrapment/post-eruptive cooling inside vapour bubbles (Fig. 10) by analogy with hydrothermal and magmatic metal/mineral ore deposits.

Evolution of magmatic C–O–H–S fluids upon cooling inside the shrinkage bubbles of MIs

In naturally quenched inclusions, the cooling history of the shrinkage bubble can be traced back from magmatic to ambient pressure and temperature conditions, whereas in re-heated MIs, volatile diffusion can be induced by homogenization experiments at magmatic temperatures (e.g. Massare *et al.*, 2002; Bodnar &

Student, 2006; Esposito, 2012). Thus, in order to investigate the early chemical evolution at high temperatures of the C–O–H–S fluid system in shrinkage bubbles of primary MIs at San Cristóbal, we considered the relationships between equilibrium temperatures and mineral parageneses identified with Raman microspectroscopy, SEM and EDS. To roughly estimate original magmatic temperatures, the olivine-liquid equilibrium geothermometer of Putirka (2008) was applied to the major element exchanges between the MI and their host crystals (Supplementary Data Electronic Appendix 3). The results yield temperatures of 1088 ± 31°C (range = 1009–1141°C) for bubble-bearing inclusions, but the ideal starting temperature could be limited to 1141°C in the cooling model of the present study (Fig. 10).

Bubble nucleation and contraction are calculated between 479–527°C (Supplementary Data Electronic Appendix 4; Giordano *et al.*, 2005), assuming that volatiles are continuously diffusing from the melt. The closure temperature for elemental diffusion during typical cooling of magmatic systems is probably the best proxy for tracking the limits of these processes (Supplementary Data Electronic Appendix 4) (e.g. Dodson, 1973), because it indicates the temperature at which a volatile phase (i.e. CO_2 or H_2O) stops diffusing in the MI (Fig. 10). The temperatures for CO_2 diffusion are given in Table 3 and Supplementary Data Electronic Appendix 4, from which, despite a low precision, it can be proposed that the temperature ranges for CO_2 migration lie in the interval between 447 and 774°C, which are markedly higher than the water minimum temperature calculated at 270°C.

Regarding the mineral equilibrium assemblages in the samples of San Cristóbal (Fig. 7, Table 5), a C–O–H–S vapour, or supercritical fluid phase could have been present before any solids were precipitated. The data discussed above indicate that the fluid composition in a C-O-H system would correspond to 32–71 mol % CO_2 and 29–68 mol % H_2O, depending on the inclusion. Sulfur could also have been present at this stage because it partitions strongly into C–H–O–S–Cl fluid(s) at various pressures, temperatures and melt compositions (Webster & Botcharnikov, 2011). However, additional experimental studies are required to constrain the sulfur diffusion coefficient from basaltic glasses (Baker *et al.*, 2005; Freda *et al.*, 2005) in order to estimate the mole fraction of sulfur species in the vapour (e.g. Esposito *et al.*, 2016) and the closure temperature.

Inside the shrinkage bubbles, the presence of pyrite implies precipitation conditions, probably involving H_2S, at maximum temperatures of ~400–742°C (Fig. 10) (Power & Fine, 1976; Lusk & Bray, 2002). Chalcopyrite was also detected at the bubble–glass rim (22 of the 31 samples) (SC02Br3; Fig. 3a–c), which should have precipitated at temperatures <568°C (Fig. 10) (Lusk & Bray, 2002). Cpy solubility decreases rapidly from 400 to 250°C (Crerar & Barnes, 1976), which are typical temperatures in a cooling magmatic-hydrothermal system (Wilkinson, 2013). Cpy was even detected with kieserite ($MgSO_4 \bullet H_2O$), which means that elemental copper and iron coexist with carbon dioxide, water, and sulfur species in the same bubble in magmatic, hydrothermal and ambient thermal conditions (Figs 10, 11a and b; Table 5). The presence of coexisting sulfates and sulfides in some bubbles provides evidence of H_2S and SO_4^{2-} in the fluid, which might indicate SO_2 disproportionation at deeper crustal levels (Rye, 2005) (Table 5).

Pyrite and chalcopyrite precipitation inside the fluid environment of the shrinkage bubble requires a significant drop in temperature after eruptive cooling down to the fluctuating conditions of the shallow plumbing system (105–582°C; Fig. 10). The temperatures inside the San Cristóbal crater are ideal for dissolving and transporting iron and copper in the conduit, as reflected by the presence of 18 μg/g Fe and 0·6 μg/g Cu in fumarole condensates, but this is particularly critical for concentrating ligands such as Cl^- and SO_4^{2-} (9000–10 500 and 1240–1480 μg/g, respectively) (Gemmell, 1987). Metals such as copper and iron may be preferentially removed from the magma to the gas phase as metal halides in these open systems (Weast & Astle, 1984; Gemmell, 1987). Alternatively, some recent models imply that deep CO_2 fluxing would efficiently change the stability of the (copper) metal complex and reduce its solubility in the water vapour before being transported (van Hinsberg *et al.*, 2016). The hypothesis of CO_2 fluxing may be supported by the major volatile contents in our MI data (Fig. 8a and b).

Chlorine could act as a transporting agent for metals, because partition coefficients at San Cristóbal indicate it is preferentially transferred to fluid phases. The estimated diffusivity of chlorine (D_{Cl}) is 6·1–7·1 cm^2/s, which is close to the reported values for experimental aqueous vapour/basaltic melts of 1 and 6 cm^2/s at 2 kbar and 1100°C (Webster, 1992; Stelling *et al.*, 2008). Chlorine plays a critical role in shallow open-system degassing in the transport of major elements (Weast & Astle, 1984; Gemmell, 1987), but its detection and concentration in the bubble environment is uncertain (melt-dissolved Cl increased by 60% with bubble size in parallel with the S and Cu contents; Fig. 8h). Halite crystals and Cl-rich alumino-silicate phases were previously observed at the bubble–glass interfaces in bubbles from MIs of MORB volcanic systems (Kamenetsky *et al.*, 2001, 2002). Conversely, at San Cristóbal, halides have not been detected inside bubbles by BSE imaging. In addition, halogen ionic bonds are very weakly Raman active, which might have prevented their detection (Burke, 2001; Frezzotti *et al.*, 2012). The amount of chlorine inside the bubble is thus unconstrained and should be further investigated under these conditions, as for some vapour-dominant fluid inclusions (Seo *et al.*, 2009), sulfur might turn out to be the principal metal-transporting ligand, but in this case inside CO_2-rich vapour bubbles.

The final cooling stages of the shrinkage bubble correspond to the lowest hydrothermal temperatures (<250°C). It was not surprising to find disordered Fe-

bearing magnesite formed under low-temperature conditions in bubbles often along with CO_2 (in 12 samples). Liquid water was also found with magnesite (in five samples), meaning that precipitation of magnesium carbonate at low temperatures (<350°C) could occur in aqueous fluids (Mackenzie *et al.*, 1983). Magnesite could be interpreted here as a result of an Mg precipitation reaction with CO_2 in the fluid, or by precipitating from an aqueous phase, such as Mg^{2+} with CO_3^{2-} at low temperatures (Table 5). Magnesite can form at ~200–300°C by hydrothermal dissolution in certain ore deposits (Oskierski *et al.*, 2013), but also at ambient temperatures as demonstrated by experimental studies in aqueous solutions (Ki *et al.*, 1973). Aqueous fluids undoubtedly represent the main reactive agents at such low-temperature conditions. The presence of a hydrous Mg sulfate in 2 of the 31 samples supports that hydrothermal reactions also involved sulfur, and confirms that a C–O–H–S fluid system evolves in shrinkage bubbles of MIs over the whole cooling history of MIs to ambient conditions.

Shrinkage bubbles: bridging the gap from volcanology to ore-deposit formation

The present results outline a significant role played by sulfur, in addition to chlorine (Kamenetsky *et al.*, 2001, 2002), in copper transport by fluids exsolved from mafic magmas (Pokrovski *et al.*, 2008; Seo *et al.*, 2009). A comparison with magmatic hydrothermal copper-mineralization models is thus proposed here to explain the paragenetic mineral sequence found inside the bubble environment of San Cristóbal MIs, although the timescales for cooling high-temperature MIs and hydrothermal deposits are distinctly different. MI systems are quenched over extremely short timescales (from a fraction of a second to a few hours), whereas the cooling systems for water–air interactions in hydrothermal deposits are prolonged and cyclic. Further, in MIs, temperatures decrease linearly, while in hydrothermal systems they fluctuate.

Present data suggest that copper might be soluble inside the closed bubble environment and preferentially partition into an immiscible, saturated magmatic fluid. Fluid immiscibility (coexisting gaseous and liquid phases) from the melt may occur during nucleation of the inclusion bubble (i.e. representing a first transport step). However, how can this happen? During the first stage of bubble formation inside the MIs, if vapour predominates, the transport analogy with vapour-dominant systems could be reflected in several magmatic and genetic models of porphyry copper deposits (e.g. Sawkins & Scherkenbach, 1981; Lowenstern *et al.*, 1991; Heinrich *et al.*, 1992, 1999; Bodnar, 1995, Williams-Jones & Heinrich, 2005; Sillitoe, 2010). This idea is supported experimentally by fluid-inclusion immiscibility processes (e.g. boiling) (Heinrich *et al.*, 1992, 1999; Audétat *et al.*, 1998). If the bubble represents a CO_2-rich microenvironment (only in four of 13 MI samples used for IGL corrections), the conditions favor a homogeneous fluid during bubble nucleation, but with our previous conceptual model (Fig. 11) we showed that the occurrence of copper deposition depends firstly on the (possibility of) fluid/melt immiscibility and post-entrapment liquid interactions at the bubble–glass interface (Fig. 11).

It is challenging to reconstruct the C–O–H–S–Cl fluid system and metal (Cu) transport at near-magmatic temperatures and upon cooling. The unusual enrichment of Cu along the bubble walls at San Cristóbal could be due to fluid saturation occurring in the immiscible fluid trapped with melts after decompression and, or, crystallization from mafic melts. This well agrees with basaltic MIs having high Fo contents (series SC11, SC5c-D; Fig. 4g and h). At higher pressures (>90 MPa) (Robidoux *et al.*, 2017), sulfide liquid saturation would also be a plausible mechanism to concentrate sulfur and chalcophile elements in the fluid, since it is already supplied by a mafic sulfur-rich melt (e.g. Hattori & Keith, 2001) (MI composition of SC11Dr1g of 2532 ± 10 μg/g by nano-SIMS) (Supplementary Data Electronic Appendix 3). Below magmatic temperatures, within the hydrothermal fluid context, it is also possible that copper precipitates in the water from the bubble environment, but an analogy with metal-rich hydrothermal fluid requires geological knowledge of the whole magma feeding system; e.g. magmatic mixing of two endmembers with different compositions (Zellmer *et al.*, 2015; Wilkinson, 2013), or the injection of mafic and chalcophile-rich magma into a shallow felsic magma in the crust, which could transfer base metals from a magmatic volatile phase (e.g. Merapi; Nadeau *et al.*, 2010).

Another mechanism to form sulfur-rich melt phases (e.g. Ebel & Naldrett, 1997; Kamenetsky & Kamenetsky, 2010; Barnes & Ripley, 2016) is based on the low modeled saturation limit for sulfur estimated in basaltic glass of bubble-bearing inclusions from San Cristóbal (1662 μg/g S; Fig. 9c) using the equation of Fortin *et al.* (2015) (Supplementary Data Electronic Appendix 4). Those saturation limits are lower than the measured sulfur content from the inclusion, which, therefore, supports this idea. It is particularly interesting that this mechanism is not typical of shrinkage bubbles in basaltic andesites, but instead is associated with larger fluid bubbles in basaltic MIs (Figs 4h and 9c).

Larger bubbles are likely to be formed by melt/fluid immiscibility processes, but this still does not explain why sulfides and sulfates formed at the bubble–glass interface in MIs of different populations (Fig. 4). Also, copper- and iron-sulfides were observed in bubbles of variable size (even pure shrinkage bubbles), independent of glass composition and bubble volume percentage (Fig. 9a). Thus, sulfur- and copper-rich mineralization does not necessarily require fluid immiscibility processes, and further petrographic evidence is required for invoking the separation of S-immiscible, Cu–Fe-rich sulfide fluids from the trapped melt inside the inclusion.

Sulfur enrichment definitively increases (by 94%) with bubble volume percentage, temperature (Fig. 11a),

and chlorine and copper abundance (Fig. 9c, e, and h) (Seo *et al.*, 2009), all related to their solubility in less differentiated basaltic melts. Sulfur contents are also inversely related to pressure (Fig. 9b) and CO_2 content (Fig. 9f and g). These correlated variables at high-temperature trapping conditions (1100°C) support the findings of recent experiments on high copper magma diffusivity (D_{Cu}) at >1300°C (Ni & Zhang, 2016), where D_{Cu} is generally higher than D_S-D_{Cl}, but smaller than D_{H2O}. In contrast, Zn (which is also chalcophile) is preferentially concentrated in differentiated MIs with a higher bubble volume percentage, implying that metal diffusion and speciation in a silicate melt is an even more complex issue during bubble formation (Fig. 9d and i). To tentatively explain the correlation of intensive variables illustrated in Fig. 9, we propose that the effect of bubble size on metal/volatile solubility and diffusion instead contributes to post-entrapment cation exchange for melt or aqueous S–Cl-rich fluids, similarly to what is observed in the chemical evolution of mixed melt–fluid inclusions (Zajacz & Halter, 2009 and references therein). We consequently propose that metal transport and S–Cl ligands are controlled by the surface contact area of the bubble–glass interface (i.e. proportional to the bubble volume percentage) and the presence of liquid water (glass hydration) during and after eruptive cooling. Additionally, chemical reactions between volatiles in the vapour and the dissolved major species in water (or a CO_2-rich fluid) occur over a temperature interval inside the shrinkage bubble during cooling (Kamenetsky *et al.*, 2007).

Therefore, the data from the San Cristóbal samples indicate that both gas and liquid are phases that remain in the bubble system and that may participate to form characteristic mineral parageneses. Some distinction can be made between eruptions, depending on the pre-eruptive to post-eruptive cooling conditions of the olivine hosts. For example, carbonates and Cpy coexist in larger vapour bubbles in basaltic MIs, whereas generally they are not observed in typically small shrinkage bubbles in basaltic andesites (Table 5). This suggests that during bubble contraction of basaltic andesitic MIs (500–527°C), SO_4^{2-} in C–O–H–S vapour/fluid can precipitate as sulfates, whereas in basalts, CO_3^{2-} anions can form magnesite (<350°C). The discovery of an aqueous component in the natural environment of shrinkage bubbles is an important finding, since it probably preserves the earliest and most-primitive stages of fluid–rock interaction in the crystallization history of an igneous body. This finding can thus provide additional information on the magmatic processes responsible for Cu–Fe sulfur mineralization in porphyry copper environments and complement data from studies of fluid inclusions (Shinohara *et al.*, 1995; Heinrich *et al.*, 1999; Williams-Jones & Heinrich, 2005; Audétat *et al.*, 2008).

CONCLUSIONS

The combined application of high-precision Raman microspectroscopy and BSE imaging has revealed the complex C–O–H–S fluid system present in shrinkage bubbles of naturally quenched MIs at San Cristóbal volcano. An extensive petrographic classification of MI texture and a revision of their composition (EMPA, nano-SIMS, and LA-ICP-MS) was necessary to construct a conceptual fluid/melt model of C–O–H–S migration from the inclusion to the bubble, from pre-eruptive to post-eruptive cooling. The main conclusions are as follows:

1. Liquid water has been detected coexisting with gaseous carbon dioxide inside natural shrinkage bubbles for the first time in naturally quenched inclusions (in seven of the 31 MIs). Combined with the findings of previous studies (Wallace *et al.*, 2015 and references therein), these results have been used to recalculate the total CO_2 contents of trapped MIs and improve geobarometers (using mass balance calculations) for locating the minimum depth of primary magma degassing below San Cristóbal (~200–425 MPa; ~5–16 km). The CO_2 Raman densimeter equations (e.g. Fall *et al.*, 2011) correspond well with the instrumental calibration/peak treatment methodology and allow accurate calculations of the CO_2 density in ten bubbles, with five being used in Raman-corrected CO_2 solubility models (Witham *et al.*, 2012).
2. The first source of error to be addressed when studying the total magmatic budget estimations at San Cristóbal is related to the divergence between the minimum (350 tons, for 5% of the olivines containing shrinkage bubbles) and maximum (8550 tons, for 100% of the olivines containing shrinkage bubbles) magmatic CO_2 budgets. This is particularly critical and implies that detailed textural studies of MIs should be performed routinely (Cannatelli *et al.*, 2016). Instrumental and methodological uncertainties linked to the CO_2 density in shrinkage bubbles are not negligible (Gaetani *et al.*, 2017; Créon *et al.*, 2018; Moore *et al.*, 2018). Water diffusion effects that have previously been commented on in relation to heating experiments (Danyushevsky *et al.*, 2002; Baker, 2008; Esposito, 2012; Esposito *et al.*, 2016; Lamadrid *et al.*, 2017; Moore *et al.*, 2018) additionally induce an error in the calculation of the CO_2 budgets. Finally, one potential error beyond petrological considerations is related to the CO_2 loss by open-vent degassing from the volcano. This has been estimated to be of about ~4–12 megatons at San Cristóbal from 1976 to 2015, based on CO_2 fluxes of ~260–786 tons/day measured by Aiuppa *et al.* (2014).
3. The Raman-corrected CO_2 content of MI bubbles should be used to study degassing paths, preferably combined with a quantitative and accurate petrological approach for estimating the original water content in the magma (e.g. Aster *et al.*, 2016). Detailed Raman-spectroscopy-based identification of solid phases inside shrinkage bubbles is necessary because they represent reaction products of a C–O–H–S vapour-fluid closed system and could introduce additional bias into solubility models of multiple

volatiles (e.g. Papale *et al.*, 2006; Iacono-Marziano *et al.*, 2012; Witham *et al.*, 2012).

4. To explain the C–O–H–S fluid/melt interaction (Kamenetsky *et al.*, 2001, 2002; Esposito *et al.*, 2014, 2016; Robidoux *et al.*, 2015*a*, *b*), intensive variables (pressure, temperature, and concentrations of volatiles) were compared with the vapour-bubble/inclusion volume ratios (bubble volume percentage). The observed correlations showed that silicate melt chemical properties may affect vapour bubble expansion/contraction rates during eruptive cooling (e.g. Roedder, 1979; Lowenstern, 1995). We propose two possible mechanisms to explain the correlations between the intensive variables and the C–O–H–S fluids inside the bubbles that lead to mineral precipitation from hydrothermal temperatures to ambient temperatures: (i) volatile diffusion and glass–fluid interactions, and (ii) the presence of immiscible fluids.
5. The minerals identified inside the bubbles include variably disordered carbonates (hydrothermal magnesite), a hydrous sulfate (kieserite type), and sulfides (pyrite, marcasite, and chalcopyrite). The C–O–H–S fluid migration from the inclusion to the vapour bubble occurred during vapour bubble nucleation, expansion, and until its contraction (400–500°C), which depends mainly on the silicate melt composition and quenching rates. Considering those properties, the cooling history inside the shrinkage bubble can be modeled starting with diffusion of volatiles (1200–250°C), then MI formation (~1100°C) and thermal precipitation conditions forming the paragenetic mineral sequence of the bubble: high-temperature sulfide precipitation (500–700°C) followed by low-temperature carbonates and hydrous sulfates (<500°C).
6. The carbonate and Mg–Fe–Cu sulfide (sulfate) mineral paragenesis indicates that a C–O–H–S fluid migrated into the shrinkage bubble. Further experimental studies are required to determine if the precise mechanism involves fluid–glass interactions (post-trapping) or if the S-metal-rich magma is saturated and exsolves an immiscible fluid during MI trapping. This last hypothesis could partially explain the occurrence of Cu–Fe sulfides in larger fluid bubbles. However, the rocks sampled at San Cristóbal do not show clear petrographic evidence of S melt immiscibility from a silicate melt at magmatic stages (e.g. at reducing conditions or during magma mixing). Water played a key role at the bubble–glass interface during and after eruptive cooling by inducing glass hydration along bubble-inclusion rims. Early igneous water-rich fluids may have reacted with Mg–Fe–Cu in the glass inclusions to form mineral phases. Similar glass–water interactions are excellent analogs to early magmatic hydrothermal interactions, which are frequently described in epithermal/porphyry copper deposit models (Hedenquist and Lowenstern, 1994; Shinohara *et al.*, 1995; Heinrich *et al.*, 1999; Williams-Jones & Heinrich, 2005; Sillitoe, 2010).

The approach presented here can be used to determine the chemical reactions of open-system fluid–rock interactions (for recent geological timescales) that affect the chemistry of fluid inclusions (often formed by secondary processes). We propose that future studies should perform heating experiments on glass inclusions to reveal if chemical reactions and fluctuating temperatures inside the bubble might induce alternating dissolution/precipitation processes that may mask early indications of the separation of an immiscible C–O–H–S fluid from the melt.

ACKNOWLEDGMENTS

Erik Hauri tragically died on September 5, 2018. This article is dedicated to his memory. Special thanks are addressed to S. Ferranda and P. Rossetti for Raman spectroscopy at the U. of Torino, Dr Gilles Lévresse and L. Créon (UNAM, CIGEOM, México), Prof. M Merli (U. Palermo) and Dr E. Oglialoro (U. Milano-Bicocca) for general discussions and improvements on data treatments. We also recognise the important contribution from A. Cavallo and P. Scarlato (INGV-Rome) for electron microprobe analysis, F. Furnari (DiSTeM) for scanning electron microscopy analysis, Dr J. Wang for nano-SIMS sample preparation at the Carnegie Institution (Washington), Dr A. Paonita and Dr A.-L. Rizzo for their help at the laboratory of INGV-Palermo. This work was possible to frame along side the recent scientific advances in petrology between 2013 and 2016, thanks to dynamic discussions with R. Esposito, Prof P. Wallace, Prof. S. Rotolo and Dr G. Lanzo.

FUNDING

Fonds de Recherche du Québec Nature et technologies (FRQNT) (Programme B2, Comité 04B, Groupe: 1) helped to support the PhD project and as part of the thesis investigation, the effort was partially financed by the Deep Carbon Observatory and received funding from the European Research Council under the European Union's Seventh Framework Programme (FP7/2007/2013)/ERC grant agreement n1305377.

SUPPLEMENTARY DATA

Supplementary data are available at *Journal of Petrology* online.

REFERENCES

Aiuppa, A., Robidoux, P., Tamburello, G., Conde, V., Galle, B., Avard, G., Bagnato, E., De Moor, J. M., Martínez, M. & Muñóz, A. (2014). The Costa Rica–Nicaragua volcanic segment: along arc variations in volcanic gas chemistry and improved CO_2 budget. *Earth and Planetary Science Letters* **407**, 134–147.

Anderson, A. T. (1974). Evidence for a picritic, volatile-rich magma beneath Mt. Shasta, California. *Journal of Petrology* **15**, 243–267.

Anderson, A. T. (1991). Hourglass inclusions: theory and application to the Bishop Rhyolitic Tuff. *American Mineralogist* **76**, 530–547.

Anderson, A. T. & Brown, G. G. (1993). CO_2 contents and formation pressures of some Kilauean melt inclusions. *American Mineralogist* **78**, 794–803.

Aster, E. (2015). *Reconstructing CO_2 concentrations in basaltic melt inclusions from mafic cinder cones using raman analysis of vapour bubbles*. M.S. thesis, Department of Geological Sciences and the Graduate School of the University of Oregon.

Aster, E. M., Wallace, P. J., Moore, L. R., Watkins, J., Gazel, E. & Bodnar, R. J. (2016). Reconstructing CO_2 concentrations in basaltic melt inclusions using Raman analysis of vapour bubbles. *Journal of Volcanology and Geothermal Research* **323**, 148–162.

Audétat, A., Günther, D., Heinrich, C. A. (1998). Formation of a magmatic-hydrothermal ore deposit: insight with LA-ICP-MS analysis of fluid inclusions. *Science* **279**, 2091–2094.

Audétat, A., Pettke, T., Heinrich, C.A., Bodnar, R.J. (2008). *Economic Geology* **103**, 877–908.

Baker, D. R. (2008). The fidelity of melt inclusions as records of melt composition. *Contributions to Mineralogy and Petrology* **156**, 377–395.

Baker, D. R., Freda, C., Brooker, R. A. & Scarlato, P. (2005). Volatile diffusion in silicate melts and its effects on melt inclusions. *Annals of Geophysics* **48**, 699–717.

Barnes, S.-J., Ripley, E. M. (2016). Highly siderophile and strongly chalcophile elements in magmatic ore deposits. *Reviews in Mineralogy and Geochemistry* **81**, 725–774.

Blundy, J., Cashman, K. V., Rust, A. & Witham, F. (2010). A case for CO_2-rich arcmagmas. *Earth and Planetary Science Letters* **290**, 289–301.

Bodnar, R. J. (1995). Fluid inclusion evidence for a magmatic source for metals in porphyry copper deposits. In Thompson, J. F. H. (ed.) *Magmas, Fluids and Ore Deposits*, Mineral Association of Canada Short Course Series 23, pp. 39–152.

Bodnar, R. J. (2003). Reequilibration of fluid Inclusions. In: Samson, I., Anderson, A. & Marshall, D. (eds) *Fluid Inclusions: Analysis and Interpretation*, **Vol. 32**. Québec: Mineralogical Association of Canada Short Course Series, pp. 213–230

Bodnar, R. J. & Student, J. J. (2006). Melt inclusions in plutonic rocks: petrography and microthermometry. *Melt Inclusions in Plutonic Rocks* **36**, 1–25.

Bolge, L. L., Carr, M. J., Milidakis, K. I., Lindsay, F. N. & Feigenson, M. D. (2009). Correlating geochemistry, tectonics, and volcanic volume along the Central American Volcanic Front. *Geochemistry Geophysics Geosystems* **10**, 1–15.

Boulard, E., Guyot, F. & Fiquet, G. (2012). The influence on Fe content on Raman spectra and unit cell parameters of magnesite–siderite solid solutions. *Physics and Chemistry of Minerals* **39**, 239–246.

Bucholz, C. E., Gaetani, G. A., Behn, M. D. & Shimizu, N. (2013). Post-entrapment modification of volatiles and oxygen fugacity in olivine-hosted melt inclusions. *Earth and Planetary Science Letters* **374**, 145–155.

Burke, E. A. J. (2001). Raman microspectrometry of fluid inclusions. *Lithos* **55**, 139–158.

Cannatelli, C., Doherty, A. L., Esposito, R., Lima, A. & De Vivo, B. (2016). Understanding a volcano through a droplet: A melt inclusión approach. *Journal of Geochemical Exploration* **171**, 4–19.

Carr, M. J. (1984). Symmetrical and segmented variation of physical and geochemical characteristics of the Central American volcanic front. *Journal of Volcanology and Geothermal Research* **20**, 231–252.

Carr, M. J., Feigenson, M. D. & Bennett, E. A. (1990). Incompatible element and isotopic evidence for tectonic control of source mixing and melt extraction along the Central American arc. *Contributions to Mineralogy and Petrology* **105**, 369–380.

Carr, M. J., Saginor, I., Alvarado, G. E., Bolge, L. L., Lindsay, F. N., Milidakis, K., Turrin, B. D., Feigenson, M. D. & Swisher, C. C. III, (2007). Element fluxes from the volcanic front of Nicaragua and Costa Rica. *Geochemistry, Geophysics, Geosystems* **8**, 1–22.

Cervantes, P., Kamenetsky, V. & Wallace, P. J. (2002). Melt inclusion volatile contents, pressures of crystallization for Hawaiian picrites, and the problem of shrinkage bubbles. In: *AGU Fall Meeting Abstracts*, **Vol. 1**, p. 1217.

Chen, Y., Provost, A., Schiano, P. & Cluzel, N. (2011). The rate of water loss from olivine- hosted melt inclusions. *Contributions to Mineralogy and Petrology* **162**, 625–636.

Clocchiatti, R. (1975). Les inclusions vitreuses des cristaux de quartz. Étude optique, thermo-optique et chimique. Applications géologiques: Mémoires de la Société Géologique de France, Nouvelle Série, 54, 1, Mémoire n. 122, Paris: Société géologique de France, 96 p.

Correale, A., Martelli, M., Paonita, A., Rizzo, A. L., Brusca, L. & Scribano, V. (2012). New evidences of mantle heterogeneity beneath the Hyblean Plateau (southeast Sicily, Italy) as inferred from noble gases and geochemistry of ultramafic xenoliths. *Lithos* **132–133**, 70–81.

Créon, L., Lévresse, G., Remusat, L., Bureau, H. & Carrasco-Nuñez, G. (2018). New method for initial composition determination of crystallized silicate melt inclusions. *Chemical Geology* **483**, 162–173.

Crerar, D. A. & Barnes, H. L. (1976). Ore solutions chemistry V. solubilities of chalcopyrite and chalcocite assemblages in hydrothermal solutions at 200°C to 350°C. *Economic Geology* **71**, 772–794.

Danyushevsky, L. V. & Plechov, P. (2011). Petrolog3: integrated software for modeling crystallization processes. *Geochemistry, Geophysics Geosystems* **12**, 1–32.

Danyushevsky, L. V., McNeill, A. W. & Sobolev, A. V. (2002). Experimental and petrological studies of melt inclusions in phenocrysts from mantle-derived magmas: an overview of techniques, advantages and complications. *Chemical Geology* **183**, 5–24.

Danyushevsky, L. V., Falloon, T. J., Sobolev, A. V., Crawford, A. J., Carroll, M. & Price, R. C. (1993). The H_2O content of basalt glasses from Southwest Pacific back-arc basins. *Earth and Planetary Science Letters* **117**, 347–362.

Demets, C. (2001). A New estimate for present-day Cocos–Caribbean plate motion: implications for slip along the Central American Volcanic Arc. *Geophysical Research Letters* **28**, 4043–4046.

Dodson, M. H. (1973). Closure temperature in cooling geochronological and petrological systems. *Contributions to Mineralogy and Petrology* **40**, 259–274.

Ebel, D. S. & Naldrett, A. J. (1997). Crystallization of sulfide liquids and the interpretation of ore composition. *Canadian Journal of Earth Sciences* **34**, 352–365.

Esposito, R. (2012). *Studies of volatile evolution in magmatic systems using melt inclusions*. Doctoral dissertation, Blacksburg, VA: Virginia Polytechnic Institute and State University.

Esposito, R., Bodnar, R. J., Danyushevsky, L. V., de Vivo, B., Fedele, L., Hunter, J., Lima, A. & Shimizu, N. (2011). Volatile evolution of magma associated with the Solchiaro eruption in the Phlegrean Volcanic District (Italy). *Journal of Petrology* **52**, 2431–2460.

Esposito, R., Hunter, J., Schiffbauer, J. D., Shimizu, N. & Bodnar, R. J. (2014). An assessment of the reliability of melt

inclusions as ecorders of the pre-eruptive volatile content of magmas. *American Mineralogist* **99**, 976–998.

Esposito, R., Lamadrid, H. M., Redi, D., Steele-MacInnis, M., Bodnar, R. J., Manning, C. E., De Vivo, B., Cannatelli, C. & Lima, A. (2016). Detection of liquid H2O in vapour bubbles in reheated melt inclusions: implications for magmatic fluid composition and volatile budgets of magmas? *American Mineralogist* 101, 1691–1695.

Fall, A., Tattitch, B. & Bodnar, R. J. (2011). Combined microthermometric and Raman spectroscopic technique to determine the salinity of H_2O–CO_2–NaCl fluid inclusions based on clathrate melting. *Geochimica et Cosmochimica Acta* **75**, 951–964.

Fermi, E., Z. (1931). Über den Ramaneffekt des Kohlendioxyds. *Zeitschrift für Physik* **71**, 250.

Fortin, M. A., Riddle, J., Desjardins-Langlais, Y. & Baker, D. R. (2015). The effect of water on the sulfur concentration at sulfide saturation (SCSS) in natural melts. *Geochimica et Cosmochimica Acta* **160**, 100–116.

Freda, C., Baker, D. R. & Scarlato, P. (2005). Sulfur diffusion in basaltic melts. *Geochimica et Cosmochimica Acta* **69**, 5061–5069.

Frezzotti, M. L. (2001). Silicate-melt inclusions in magmatic rocks: applications to petrology. *Lithos* **55**, 273–299.

Frezzotti, M. L., Tecce, F. & Casagli, A. (2012). Raman spectroscopy for fluid inclusion analysis. *Journal of Geochemical Exploration* **112**, 1–20.

Gaetani, G. A., O'Leary, J. A., Shimizu, N., Bucholz, C. E. & Newville, M. (2012). Rapid Re-equilibration of water and oxygen fugacity in olivine-hosted melt inclusions. *Geology* **40**, 915–918.

Gaetani, G. A., Le Roux, V., Klein, F., Moore, L. R., Bodnar, R. J. & Maclennan, J. (2017). X-ray microtomography-based reconstruction of total CO_2 in olivine-hosted melt inclusions. *Goldschmidt* 2017 Abstract.

Gemmell, J. B. (1987). Geochemistry of metallic trace elements in fumarolic condensates from Nicaraguan and Costa Rican volcanoes. *Journal of Volcanology and Geothermal Research* **33**, 161–181.

Giordano, D., Nichols, A. R. L., Dingwell, D. B. (2005). Glass transition temperatures of natural hydrous melts: a relationship with shear viscosity and implications for the welding process. *Journal of Volcanology and Geothermal Research*, **142**, 105–118.

Goldstein, R. H. (1993). Fluid inclusions as microfabrics: a petrographic method to determine diagenetic history. In: Rezak, R. & Lavoi, D. (eds) *Carbonate Microfabrics. Frontiers in Sedimentary Geology*. New York: Springer-Verlag, pp. 279–290.

Goldstein, R. H. & Reynolds, T. J. (1994). Systematics of fluid inclusions in diagenetic minerals. *SEPM Short Course Notes* **31**, 199.

Goldstein, R. H. (2003). Petrographic analysis of fluid inclusions. In: Samson, I., Anderson, A. & Marshall, D. (eds) *Fluid Inclusions: Analysis and Interpretation*. Mineralogical Association of Canada, pp. 9–53.

Hartley, M. E., Maclennan, J., Edmonds, M. & Thordarson, T. (2014). Reconstructing the deep CO_2 degassing behaviour of large basaltic fissure eruptions. *Earth and Planetary Science Letters* **393**, 120–131.

Hartley, M. E., Neave, D. A., Maclennan, J., Edmonds, M. & Thordarson, T. (2015). Diffusive over-hydration of olivine-hosted melt inclusions. *Earth and Planetary Science Letters* **425**, 168–178.

Hattori, K. H., & Keith, J. D. (2001). Contribution of mafic melt to porphyry copper mineralization: evidence from Mount Pinatubo, Philippines and Bingham Canyon, Utah, USA. *Mineralium Deposita* **36**, 799–801

Hauri, H. E., Wang, J., Dixon, J. E., King, P. L., Mandeville, C. & Newman, S. (2002). SIMS analysis of volatiles in silicate glasses. *Chemical Geology* **183**, 99–114.

Havlicek, P., Hradecky, P., Hrubes, M., MIcoch, B., Opletal, M., Sebesta, J., Buitrago, N. & Strauch, W. (1999). *Estudio Geológico Y Reconocimiento De La Amenaza Natural - Zona Chinandega-Leon, Nicaragua. Praga-Managua 1999*, Resumen Ejecutivo (Servicio Geológico Checo, CGU, en cooperación con Instituto Nicaragüense de Estudios Territoriales, INETER), 23 p.

Havlicek, P., Hradecky, P., Hrubes, M., Kyel, P., MIcoch, B., Mrazova, S., Novak, Z., Opletal, M., Prichystal, A., Sebesta, J., Seveik, J., Bustillo, M. & Rizo, Z. (2000). *Estudio Geológico Y Reconocimiento De La Amenaza Geológica En El Área De León - La Paz Centro Y Malpasillo, Praga-Managua 2000*, Reporte Final (Servicio Geológico Checo, CGU, en cooperación con Instituto Nicaragüense de Estudios Territoriales, INETER), 244 p.

Hazlett, R. W. (1977). *Geology and Hazards of the San Cristobal Volcanic Complex*. Nicaragua: Darmouth College, 212 p.

Hazlett, R. W. (1987). Geology of the San Cristobal volcanic complex, Nicaragua. *Journal of Volcanology and Geothermal Research* **33**, 223–230.

Hedenquist, J. W. & Lowenstern, J. B. (1994). The role of magmas in the formation of hydrothermal ore deposits. *Nature* **370**, 519–527.

Heinrich, C. A., Günther, D., Audétat, A., Ulrich, T. & Frischknecht, R. (1999). Metal fractionation between magmatic brine and vapour, determined by microanalysis of fluid inclusions. *Geology* **27**, 755–758.

Heinrich, C. A., Ryan, C. G., Mernagh, T. P. & Eadington, P. J. (1992). Segregation of ore metals between magmatic brine and vapour—a fluid inclusion study using PIXE microanalysis. *Economic Geology* **87**, 1566–1583.

Heydolph, K., Hoernle, K., Hauff, F., Bogaard, P V D., Portnyagin, M., Bindeman, I. & Garbe-Schönberg, D. (2012). Along and across arc geochemical variations in NW Central America: evidence for involvement of lithospheric pyroxenite. *Geochimica et Cosmochimica Acta* **84**, 459–491.

Iacono-Marziano, G., Morizet, Y., Trong, E. L. and Gaillard, F. (2012). New experimental data and semi empirical parameterization of H_2O–CO_2 solubility in mafic melts. *Geochimica et Cosmochimica Acta*, **97**, 1–23.

INETER (Instituto Nicaragüense de Estudios Territoriales) (2014). *Geofísica en Nicaragua – Boletines Sismológicos*. .

Johnson, E. R., Wallace, P. J., Cashman, K. V. & Delgado-Granados, H. (2010). Degassing of volatiles (H_2O, CO_2, S, Cl) during ascent, crystallization, and eruption at mafic monogenetic volcanoes in central Mexico. *Journal of Volcanology and Geothermal Research* **197**, 225–238.

Kamenetsky, V. S., Binns, R. A., Gemmell, J. B., Crawford, A. J., Mernagh, T. P., Maas, R. & Steele, D. (2001). Parental basaltic melts and fluids in eastern Manus backarc basin: implications for hydrothermal mineralization. *Earth and Planetary Science Letters* **184**, 685–702.

Kamenetsky, V. S., Davidson, P., Mernagh, T. P., Crawford, A. J., Gemmell, J. B., Portnyagin, M. V. & Shinjo, R. (2002). Fluid bubbles in melt inclusions and pillow-rim glasses: high temperature precursors to hydrothermal fluids? *Chemical Geology* **183**, 349–364.

Kamenetsky, V. S. & Kamenetsky, M. B. (2010). Magmatic fluids immiscible with silicate melts: examples from inclusions in phenocrysts and glasses, and implications for magma evolution and metal transport. *Geofluids* **10**, 293–311.

Kamenetsky, V. S., Pompilio, M., Métrich, N., Sobolev, A. V., Kuzmin, D. V. & Thomas, R. (2007). Arrival of extremely

volatile-rich high-Mg magmas changes explosivity of Mount Etna. *Geology* **35**, 255–258.

Kawakami, Y., Yamamoto, J. & Kagi, H. (2003). Micro-Raman densimeter for CO_2 inclusions in mantle-derived minerals. *Applied Spectroscopy* **57**, 1333–1339.

Ki, D. O., Morikawa, H., Iwai, S.-I. & Aoki, H. (1973). Hydrothermal growth of Magnesite Single Crystals. *American Mineralogist* **58**, 339–340.

Lamadrid, H. M., Moore, L. R., Moncada, D., Rimstidt, J. D., Burruss, R. C. & Bodnar, R. J. (2017). Reassessment of the Raman CO_2 densimeter. *Chemical Geology* **450**, 210–222.

Lloyd, A. S., Plank, T., Ruprecht, P., Hauri, E. H. & Rose, W. (2013). Volatile loss from melt inclusions in pyroclasts of differing sizes. *Contributions to Mineralogy and Petrology* **165**, 129–153.

Lowenstern, J. B. (1994). Dissolved volatile concentrations in an ore-forming magma. *Geology* **22**, 893–896.

Lowenstern, J. B. (1995). Applications of silicate-melt inclusions to the study of magmatic volatiles. *Magma, Fluids, and Ore Deposits* **23**, 71–99.

Lowenstern, J. B. (2001). Carbon dioxide in magmas and implications for hydrothermal systems. *Mineralium Deposita* **36**, 490–502.

Lowenstern, J. B. (2015). Bursting the bubble of melt inclusions. *American Mineralogist* **100**, 672–673.

Lowenstern, J. B., Mahood, G. A., Rivers, M. L. & Sutton, S. R. (1991). Evidence For extreme partitioning of copper into a magmatic vapour-phase. *Science (New York, N.Y.)* **252**, 1405–1409.

Lusk, J. & Bray, D. M. (2002). Phase relations and the electrochemical determination of sulfur fugacity for selected reactions in the Cu–Fe–S and Fe–S systems at 1 bar and temperatures between 185 and 460 C. *Chemical Geology* **192**, 227–248.

Mackenzie, F. T., Bischoff, W. D., Bishop, F. C., Loijens, M., Schoonmaker, J. & Wollast, R. (1983). Magnesian calcites; low-temperature occurrence, solubility and solid-solution behavior. *Reviews in Mineralogy and Geochemistry* **11**, 97–144.

Martinez, M. & Viramonte, J. G. (1971). *Geologia de la Cordillera Marrabios*. Catastro e Inventario de Recursos Naturales, Managua, Nicaragua

Massare, D., Métrich, N. & Clocchiatti, R. (2002). High-temperature experiments on silicate melt inclusions in olivine at 1 atm: inference on temperatures of homogenization and H_2O concentrations. *Chemical Geology* **183**, 87–98.

McBirney, A. R. & Williams, H. (1965). Volcanic History of Nicaragua. Pub. Geol. Sci., University of California, Berkeley, California, vol. 55, 73 pp.

Métrich, N. & Wallace, P. J. (2008). Volatile abundances in basaltic magmas and their degassing paths tracked by melt inclusions. *Reviews in Mineralogy and Geochemistry* **69**, 363–402.

Mironov, N. L. & Portnyagin, M. V. (2011). H_2O and CO_2 in parental magmas of Kliuchevskoi volcano inferred from study of melt and fluid inclusions in olivine. *Russian Geology and Geophysics* **52**, 1353–1367.

Mironov, N., Portnyagin, M., Botcharnikov, R., Gurenko, A., Hoernle, K. & Holtz, F. (2015). Quantification of the CO_2 budget and H_2O–CO_2 systematics in subduction-zone magmas through the experimental hydration of melt inclusions in olivine at high H_2O pressure. *Earth and Planetary Science Letters* **425**, 1–11.

Moore, L., Gazel, E., Tuohy, R., Lloyd, A., Esposito, R., Steele-MacInnis, M., Hauri, E. H., Wallace, P. J., Plank, T. & Bodnar, R. J. (2015). Bubbles matter: an assessment of the contribution of vapour bubbles to melt inclusion volatile budgets. *American Mineralogist* **100**, 806–823.

Moore, L. R., Mironov, N., Portnyagin, M., Gazel, E. & Bodnar, R. J. (2018). Volatile contents of primitive bubble-bearing melt inclusions from Klyuchevskoy volcano, Kamchatka: Comparison of volatile contents determined by mass-balance versus experimental homogenization. *Journal of Volcanology and Geothermal Research* **358**, 124–131.

Nadeau, O., Williams-Jones, A. E. & Stix, J. (2010). Sulphide magma as a source of metals in arc-related magmatic hydrothermal ore fluids. *Nature Geoscience* **3**, 501–505.

Ni, P. & Zhang, Y. (2016). Cu diffusion in a basaltic melt. *American Mineralogist* **101**, 1474–1482.

Oskierski, H. C., Bailey, J. G., Kennedy, E. M., Jacobsen, G., Ashley, P. M. & Dlugogorski, B. Z. (2013). Formation of weathering-derived magnesite deposits in the New England Orogen, New South Wales, Australia: implications from mineralogy, geochemistry and genesis of the Attunga magnesite deposit. *Mineralium Deposita* **48**, 525–541.

Papale, P., Moretti, R. & Barbato, D. (2006). The compositional dependence of the saturation surface of H_2O-CO_2 fluids in silicate melts. *Chemical Geology* **229**, 78–95.

Patino, L. C., Carr, M. J. & Feigenson, M. D. (2000). Local and regional variations in Central American arc lavas controlled by variations in subducted sediment input. *Contributions to Mineralogy and Petrology* **138**, 265–283.

Plank, T., Kelley, K. A., Zimmer, M. M., Hauri, E. H. & Wallace, P. J. (2013). Why do mafic arc magmas contain ~4 wt% water on average? *Earth and Planetary Science Letters* **364**, 168–179.

Pokrovski, G. S., Borisova, A. Y. & Harrichoury, J.-C. (2008). The effect of sulfur on vapour-liquid fractionation of metals in hydrothermal systems. *Earth and Planetary Science Letters* **266**, 345–362.

Power, L. F. & Fine, H. A. (1976). The iron-sulphur system. *Minerals Science and Engineering* **8**, 106–128.

Putirka, K. (2008). Thermometers and barometers for volcanic systems. In: Putirka, K. D., & Tepley, G. J., III (eds) *Minerals, Inclusions and Magmatic Processes. Reviews in Mineralogy and Geochemistry 69*. Chantilly, VA: Mineralogic Society of America, pp. 61–120

Qin, Z., Lu, F. & Anderson, A. T. (1992). Diffusive reequilibration of melt and fluid inclusions. *American Mineralogist* **77**, 565–576.

Riker, J. (2005). The 1859 Eruption of Mauna Loa Volcano, Hawaii: Controls on the Development of Long Lava Channels, Master's thesis, University of Oregon, Eugene.

Robidoux, P. (2016). *The nature and source of major magmatic volatiles: open-vent degassing volcanoes in the Central American Volcanic Arc.* Ph.D thesis, Dottorato di ricerca in Scienze della Terra–Indirizzo Geochimica Dipartimento di Scienze della Terra e del Mare (DiSTeM) Sez. Chimica e Fisica della Terra, 221 p. .

Robidoux, P., Aiuppa, A., Rotolo, S., Hauri, E. H., Frezzotti, M.-L. & Giudice, G. (2015a). *Refining the approach for volcanic CO_2 output estimation at San Cristóbal volcano, Oral Presentation, Goldschmidt 2015*, Pragua, Czeq. Rep. (August 2015)

Robidoux, P., Aiuppa, A., Rotolo, S., Hauri, E. H., Rizzo, A.-L. & Frezzotti, M. L. (2017). The volatile content of mafic-to-intermediate magmas from San Cristóbal volcano, Nicaragua. *Lithos* **272–273**, 147–163.

Robidoux, P., Frezzotti, M.-L., Hauri, E. H. & Aiuppa, A. (2015b). *Low-temperature superficial chemical changes and postentrapment effects alter CO2 budget estimation in vapour bubbles of glass inclusions; Poster Presentation*, AGU Meeting 2015, San Francisco, United States (December 2015).

Roedder, E. (1979). Origin and significance of magmatic inclusions. *Bull. Minéral* **102**, 487–510.

Roedder, E. (1984). Fluid inclusions, P. H. Ribbe (Ed.). Washington, DC: Mineralogical Society of America, Reviews in Mineralogy, Vol. 12, pp. 12–45.

Rosso, K. M. & Bodnar, R. J. (1995). Microthermometric and Raman spectroscopic detectionlimits of CO_2 in fluid inclusions and the Raman spectroscopic characterization of CO2. *Geochimica et Cosmochimica Acta* **59**, 3961–3975.

Sadofsky, S. J., Portnyagin, M. V., Hoernle, K. & van den Bogaard, P. (2008). Subduction cycling of volatile and trace elements through the Central American volcanic arc: evidence from melt inclusions. *Contributions to Mineralogy and Petrology* **155**, 433–456.

Sawkins, F. J. & Scherkenbach, D. A. (1981). High copper content of fluid inclusions in quartz from northern Sonora: implications for ore genesis theory. *Geology* **9**, 37–40.

Seo, J. H., Guillong, M. & Heinrich, C. A. (2009). The role of sulfur in the formation of magmatic-hydrothermal copper-gold deposits. *Earth and Planetary Science Letters* **282**, 323–328.

Shinohara, H., Kazahaya, K. & Lowenstern, J. B. (1995). Volatile transport in a convecting magma column: implications for porphyry Mo mineralization. *Geology* **23**, 1091–1094.

Sillitoe, R. H. (2010). Porphyry copper systems. *Economic Geology* **105**, 3–41.

Sisson, T. W. & Layne, G. D. (1993). H_2O in basalt and basaltic andesite glass inclusions from four subduction-related volcanoes. *Earth and Planetary Science Letters* **117**, 619–635.

Skirius, C. M., Peterson, J. W. & Anderson, A. T. (1990). Homogenizing rhyolitic glass inclusions from the Bishop Tuff. *American Mineralogist* **75**, 1381–1398.

Sobolev, A. V. & Chaussidon, M. (1996). H_2O concentrations in primary melts from supra-subduction zones and mid-ocean ridges: implications for H_2O storage and recycling in the mantle. *Earth and Planetary Science Letters* **137**, 45–55.

Sobolev, A. V. & Danyushevsky, L. V. (1994). Petrology and geochemistry of boninites from the north termination of the Tonga Trench: constraints on the generation conditions of primary high-Ca boninite magmas. *Journal of Petrology* **35**, 1183–1211.

Sobolev, V. S. & Kostyuk, V. P. (1975). Magmatic crystallization based on a study of melt inclusions. *Fluid Inclusion Research* **9**, 182–253.

Song, Y., Chou, I. M., Hu, W., Burruss, R. C. & Lu, W. (2009). CO_2 density-Raman shift relation derived from synthetic inclusions in fused silica capillaries and its application. *Acta Geologica Sinica - English Edition* **83**, 932–938.

Steele-MacInnis, M., Esposito, R. & Bodnar, R. J. (2011). Thermodynamic model for the effect of post-entrapment crystallization on the H_2O–CO_2 systematics of vapour-saturated, silicate melt inclusions. *Journal of Petrology* **52**, 2461–2482.

Stelling, J., Botcharnikov, R. E., Beermann, O. & Nowak, M. (2008). Solubility of H_2O-and chlorine-bearing fluids in basaltic melt of Mount Etna at $T = 1050$–1250 C and $P = 200$ MPa. *Chemical Geology* **256**, 102–110.

Stoiber, R. E. (2001). Fom the Papers of Richard E. Stoiber (1911-2001), Rauner Special Collections, Rauner Manuscript ML-98, Series 4, Volcano Studies, 1925-1999, Box 6, Folder 28, Darmouth College Library p. 6/7.

Thomas, R., Kamenetsky, V. S. & Davidson, P. (2006). Laser Raman spectroscopic measurements of water in unexposed glass inclusions. *American Mineralogist* **91**, 467–470.

Tuohy, R. M., Wallace, P. J., Loewen, M. W., Swanson, D. A. & Kent, A. J. (2016). Magma transport and olivine crystallization depths in Kīlauea's east rift zone inferred from experimentally rehomogenized melt inclusions. *Geochimica et Cosmochimica Acta* **185**, 232–250.

Van Hinsberg, V. J., Berlo, K., Migdisov, A. A. & Williams-Jones, A. E. (2016). CO_2-fluxing collapses metal mobility in magmatic vapour. *Geochemical Perspectives Letters* 824 (LA-UR–15-28200)

Walker, J. A., Patino, L. C., Michael, C. & Feigenson, M. D. (2001). Slab control over HFSE depletions in central Nicaragua. *Earth and Planetary Science Letters* **192**, 533–543.

Wallace, P. J., Kamenetsky, V. S. & Cervantes, P. (2015). Melt inclusion CO_2 contents, pressures of olivine crystallization, and the problem of shrinkage bubbles. *American Mineralogist* **100**, 787–794.

Walrafen, G. E. (1964). Raman spectral studies of water structure. *Journal of Chemical Physics* **40**, 3249–3256.

Walrafen, G. E. (1967). Raman spectral studies of effects of temperature on water structure. *Journal of Chemical Physics* **47**, 114–126.

Wang, X., Ming-Chou, I., Hu, W., Burrus, R. C., Sun, Q., Song, Y. (2011). Raman spectroscopic measurements of CO_2 density: experimental calibration with high-pressure optical cell (HPOC) and fused silica capillary capsule (FSCC) with application to fluid inclusion observations. *Geochimica et Cosmochimica Acta* **75**, 4080–4093.

Watson, E. B. (1991). Diffusion of dissolved CO_2 and Cl in hydrous silicic to intermediate magmas. *Geochimica et Cosmochimica Acta* **55**, 1897–1902.

Weast, R. C. & Astle, M. J. (1984). *Handbook of Chemistry and Physics*, 65th edn. Boca Raton, Fl: CRC Press, pp. D195–D199

Webster, J. D. (1992). Fluid-melt interactions involving Cl-rich granites: experimental study from 2 to 8 kbar. *Geochimica et Cosmochimica Acta* **56**, 659–678.

Webster, J. D. & Botcharnikov, R. E. (2011). Distribution of sulfur between melt and fluid in SOHC-Cl-bearing magmatic systems at shallow crustal pressures and temperatures. *Reviews in Mineralogy and Geochemistry* **73**, 247–283.

Wright, R. B. & Wang, C. H. (1973). Density effect on the Fermi resonance in gaseous CO_2 by Raman scattering. *The Journal of Chemical Physics* **58**, 2893–2895.

Wright, R. B. & Wang, C. H. (1975). Effect of density on the Raman scattering of molecular fluids. II. Study of intermolecular interactions in CO_2. *The Journal of Chemical Physics* **61**, 2707–2710.

Wilkinson, J. J. (2013). Triggers for the formation of porphyry ore deposits in magmatic arcs. *Nature Geoscience* **6**, 917–925.

Williams-Jones, A. E. & Heinrich, C. A. (2005). 100th anniversary special paper: vapour transport of metals and the formation of magmatic-hydrothermal ore deposits. *Economic Geology, Bulletin of the Society of Economic Geologists* **100**, 1287–1312.

Witham, F., Blundy, J., Kohn, S. C., Lesne, P., Dixon, J., Churakov, S. V., Botcharnikov, R. (2012). SolEx: a model for mixed COHSCL-volatile solubilities and exsolved gas compositions in basalt. *Computers & Geosciences* **45**, 87–97.

Yamamoto, J. & Kagi, H. (2006). Extended micro-Raman densimeter for CO_2 applicable to mantle-originated fluid inclusions. *Chemistry Letters* **35**, 610–611.

Yang, K. H. & Scott, S. D. (1996). Possible contribution of a metal-rich magmatic fluid to a sea-floor hydrothermal system. *Nature* **383**, 420–423.

Zajacz, Z. & Halter, W. (2009). Copper transport by high temperature, sulfur-rich magmatic vapour: evidence from silicate melt and vapour inclusions in a basaltic andesite from the Villarrica volcano (Chile). *Earth and Planetary Science Letters* **282**, 115–121.

Zellmer, G. F., Edmonds, M., & Straub, S. M. (eds) (2015). *The Role of Volatiles in the Genesis, Evolution and Eruption of Arc Magmas*. London: The Geological Society 410

Zhang, Y. (2010). Diffusion in minerals and melts: theoretical background. *Reviews in Mineralogy and Geochemistry* **72**, 5–59.

Zhang, Y. & Stolper, E. M. (1991). Water diffusion in basaltic melts. *Nature* **351**, 306–309.